PRESSURES OF PARTIAL CRYSTALLIZATION AND MAGMA PLUMBING SYSTEMS BENEATH HAWAIIAN VOLCANOES

Undergraduate Research Thesis
Submitted in partial fulfillment of the requirements for graduation
with research distinction in Earth Sciences
in the undergraduate colleges of
The Ohio State University

By

Yuyu Li
The Ohio State University
2017

Approved by

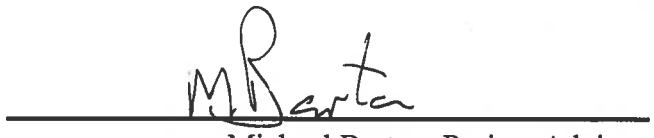

Michael Barton, Project Advisor
School of Earth Sciences

TABLE OF CONTENTS

Abstract……..ii

Acknowledgements……iii

List of Figures……iv

List of Tables……..v

Introduction……1

Geologic Setting……3

Methods

Determining Pressure of Crystallization……..8

Uncertainty……..9

Converting Pressure to Depth…..9

Samples……11

Results……18

Discussion

Data Filtration……22

Effect of Mg-Fe Exchange in Melt Inclusions……..33

Possible Interpretation of Pressure……38

Depth of Magma Chamber……39

Interpretation of Plumbing Systems……50

Conclusions……..56

Suggestions for Future Research……..57

References Cited……58

ABSTRACT

To interpret the plumbing systems beneath Hawaiian volcanoes, we have calculated the pressures of partial crystallization of basaltic magmas using the petrological method described by Kelly & Barton (2008). A total of 1576 major oxide analyses of glasses from four volcanoes (Kilauea and the Puna Ridge, Loihi, Mauna Loa, and Mauna Kea, on the Big Island) were compiled and used as input data. Glasses represent quenched liquid compositions rather than mixtures of crystals and melts, and therefore glass analyses are preferable to whole-rock analyses for calculation of pressures of partial crystallization. The results were filtered to exclude samples that yielded unrealistic results based on large errors associated with the calculated pressure or a negative value of pressure, and to exclude samples with non-basaltic compositions or those that did not lie along the liquid, olivine, plagioclase and clinopyroxene cotectic. Calculated pressures were converted to depths of partial crystallization. The majority (68.2%) of pressures of partial crystallization for the shield-stage subaerial lavas from Kilauea, Mauna Loa, and Mauna Kea, fell in the range 0–140 MPa, corresponding to depths of 0–5 km. Glasses from the Puna Ridge yielded pressures ranging from 18 to 126 MPa and were virtually identical to pressures determined from glasses from Kilauea (0–129 MPa), as expected because the Puna Ridge is an offshore extension of the East Rift zone of Kilauea. These results are consistent with the presence of magma reservoirs at depths of 0–5 km beneath the large shield volcanoes. The inferred depth of the magma reservoir beneath the summit of Kilauea (average = 1.8 km, maximum = 5 km) agrees well with depths (~2–6 km) estimated from seismic studies (Dzurisin et al, 1984). The results for Kilauea and Mauna Kea indicated that significant partial crystallization also occurs beneath the summit reservoirs at depths up to 11 km. These results are also consistent with seismic evidence for the presence of a magma reservoir at 8–11 km beneath Kilauea (Lin et al., 2014) at the base of the volcanic pile. The results for Loihi (100–400 MPa) indicate crystallization at higher average pressures and depths (3–14 km) than the large shield volcanoes, suggesting that the plumbing system is not yet fully developed, and that the Hawaiian volcanic plumbing systems evolve over time.

ACKNOWLEDGEMENTS

I would like to thank my family for their support on my college and everything I that I've been trying to do. They continue to support me to make decisions and explore the new areas. Without their support, I would never have the chance to study abroad in my current college and made everything this far. I am especially grateful to my father for his dedication and inspiration to me. He always encourages me to pursue my goal with passion and overcome difficulties in my life with giving me advice in many crucial moments. Without his encouragement, my graduation and my thesis would not be possible.

I would also like to express my gratitude to the School of Earth Sciences at The Ohio State University. Specifically, I am thankful to Dr. Anne Carey for getting me involved in the Shell Undergraduate Research Experience and providing me advice, and Dr. Karen Royce for answering so many questions about fulfilling my degree in Earth Sciences. And I would also like to thank to Shell Exploration and Production Company for funding my Shell Undergraduate Research Experience. And thanks to Friends of Orton Hall Fund for helping me to present my poster of this research in GSA and AGU meeting.

Finally, I would like to give special thanks to my advisor, Dr. Michael Barton, for providing me with opportunity to start this research topic and for inspiring and helping me to undertake this project. And I would also like to thank Jameson Scott, for helping me with using software and doing data analysis. I am deeply thankful to all the help and support from all of you.

LIST OF FIGURES

1. Topographic map of the Big Island of Hawaii in Hawaiian Emperor Seamount Chain.
2. Eight major islands in Hawaiian island chain fed by the inferred mantle plume.
3. Topographic map showing the Kea and Loa trends through eight major islands.
4. Topographic map of Kilauea, showing eruptive centers on the east rift zone.
5. Basalt tetrahedron and olivine-clinopyroxene-quartz pseudoternary plane
6. Total Alkali Silica (TAS) diagram showing compositions of glasses of five localities.
7. Total Alkali Silica (TAS) diagram showing compositions of glasses from Kilauea.
8. P vs MgO diagrams showing unfiltered results of pressure of five localities.
9. Variation diagrams of CaO vs MgO, Al_2O_3 vs MgO, CaO/Al_2O_3 vs MgO and pressure vs MgO for samples from Kilauea (without Puna Ridge)
10. Variation diagrams of CaO vs MgO, Al_2O_3 vs MgO, CaO/Al_2O_3 vs MgO and pressure vs MgO for samples from Puna Ridge.
11. Variation diagrams of CaO vs MgO, Al_2O_3 vs MgO, CaO/Al_2O_3 vs MgO and pressure vs MgO for samples from Lo'ihi.
12. Variation diagrams of CaO vs MgO, Al_2O_3 vs MgO, CaO/Al_2O_3 vs MgO and pressure vs MgO for samples Mauna Kea
13. Variation diagrams of CaO vs MgO, Al_2O_3 vs MgO, CaO/Al_2O_3 vs MgO and pressure vs MgO for samples from Mauna Loa.
14. Variation diagrams of CaO vs MgO summarizing data filtration in five steps.
15. FeO* (wt. % total Fe as FeO) vs MgO of all samples from 6 locations.
16. FeO* (wt. % total Fe as FeO) vs MgO of all samples from Mauna Loa.
17. FeO* (wt. % total Fe as FeO) vs MgO of filtered samples from 6 locations.
18. FeO* (wt. % total Fe as FeO) vs MgO of filtered samples from Mauna Loa.
19. Pressure and depth vs MgO diagrams showing filtered results of five localities.
20. Pressure and depth vs MgO diagrams showing error bar of single sample.
21. Histogram of calculated depth results for five localities.
22. Pressure and depth vs MgO diagrams of eruptive centers of Kilauea.
23. Range of depth of various eruptive centers of Kilauea, arrange by distance from summit caldera.
24. Northward-directed cut view of internal structure of Kilauea.

LIST OF TABLES

1. Sources and number of samples of each volcano on Island of Hawaii.
2. Sources and number of samples of eruptive center of Kilauea.
3. Number of each magma type from different volcanoes.
4. Number and percentage of negative pressure results from different volcanoes.
5. Number and percentage of results with high error of calculated pressure.
6. Number of results that are filtered out in each step of data filtration.
7. Average, maximum, minimum, range of majority, and average error of pressure of different volcanoes.
8. Average, maximum, minimum, range of majority, and average error of depth of different volcanoes.
9. Average, maximum, minimum of pressure and depth of different eruptive centers of Kilauea.

INTRODUCTION

The Island of Hawaii is an ideal place for studying the structure of active magmatic systems because Hawaiian volcanoes are isolated from the complications of continental processes (Ryan, 1988). Kilauea, one of the world's most active volcanoes, is located on the Big Island and its volcanic structure includes a summit caldera and two rift zones, and has been studied by various methods. The depth of magma chambers is a significant aspect to study because the depth of the magma reservoir is associated with many factors that affect volcanic hazards, for example, the eruption likelihood, duration, and styles of eruption, and its role in triggering large landslides or caldera collapses (Becerril et al., 2013). The depth of magma chambers is also an important factor to identify the thermal structure and the circulation pattern of fluid around in geothermal systems and around the magma chambers themselves. Such studies could be important for locating deep geothermal resources (Tomiya, 2000).

Seismic methods are commonly used to monitor earthquake activity associated with volcanism and to identify regions of anomalous velocities that may signify magma bodies. Monitoring of seismicity combined with measurements of ground deformation has been used for short-term eruption forecasting (Tilling & Heliker, 2010). In recent years, geodetic methods, GPS and the satellite based tool, InSAR, have been increasingly used to measure changes in ground movement of active volcanoes, both over large areas and at specific locations (Tilling & Heliker, 2010). Both geophysical and geodetic methods can provide information of the depth of magma chambers beneath active volcanoes, but petrologic methods are able to estimate the depth of chambers beneath both active and inactive volcanoes (Kelly & Barton, 2008). Moreover, estimation of depth of magma crystallization with petrologic methods provides information useful not only to establish the magma reservoir distribution but also to understand the nature of magmatic processes operating in the reservoirs (Nimis, 1995).

On the Island of Hawaii, there only three currently active volcanoes—Mauna Loa (last eruption 1984), Kilauea (ongoing eruptions since 1983), and Lo'ihi (last eruption in 1996). Mauna Kea, Haleakala, and Halalai are dormant whereas Kohala (the oldest volcano) is believed to be extinct (Wright & Pierson, 1992; Wolfe et al., 1997; Garcia et al., 1998). Lo'ihi is still a seamount, lying at 980 m below sea level, so that most previous studies of magma chambers beneath the Island of Hawaii used geophysical and geodetic methods to focus on the two subaerial shield volcanoes, Mauna Loa and Kilauea. Many petrologic studies have been done on Hawaiian lavas, and most have focused on the magma evolution although some have estimated the depth of magma chambers beneath Hawaii. However, the results for depths of magma chambers are mostly qualitative. The approach followed in this research uses the quantitative method described by Kelly & Barton (2008), in which pressure and temperature are calculated from liquid compositions in equilibrium with olivine, plagioclase, and clinopyroxene. The pressure of magma partial crystallization is calculated to an accuracy of ±126 MPa, and pressures are converted to depths using the density of basalt lava (Kelly & Barton, 2008).

The depth of magma chambers beneath four volcanoes on the Island of Hawaii, Mauna Kea, Mauna Loa, Kilauea (including the eastward extension of east rift zone, Puna Ridge), and Lo'ihi are estimated in this study based on the major element analyses of glasses that were compiled from published and unpublished sources. Data from Kilauea also included recorded locations and times of eruption (from the summit to Puna Ridge), so that samples from Kilauea along the east rift zone are arranged by distance from the summit caldera. The resulting estimates of depth are

compared with available results from geophysical, geodetic (mainly on Kilauea), and previous petrologic studies, and agree well with these results if the errors in the calculations (126 MPa) are taken into account. Some aspects of chemical composition of the erupted magmas and the implications for magma evolution related to the structure and depth of magma chambers are also discussed.

GEOLOGIC SETTING

The Hawaiian Islands (Figure 1) lie at the southeastern end of the Hawaiian Emperor Seamount Chain that stretches nearly 6000 km and encompasses at least 107 individual volcanoes (Clague & Dalrymple, 1987). The bend between the Hawaiian and Emperor segments of the chain is caused by the change of direction of Pacific Plate Motion (northward to northwestward) at ~43–45 Ma (Clague & Dalrymple, 1987). The volcanoes on the islands are formed by eruptions fed by the heat of Hawaiian mantle plume or "hot spot" as the Pacific Plate progressively moves northwestward over the hot spot. Although it is possible that plumes migrate slowly over large intervals of geologic time, their positions are relatively fixed compared with the faster motion of plates. Melting occurs in the rising plumes below the overriding plates to produce magma that is less dense than the surrounding rock and will rise by buoyancy through structurally weak zones and finally erupt to form the volcanic islands (Tilling & Heliker, 2010). The deep magmatic source of Hawaiian volcanoes, the Hawaii mantle plume, is characterized by a large flux as measured by the topographic swell, extends down to a depth of at least 2350 km and possibly as deep as 2800 km (the lowermost mantle). The plume radius is ~300 km, as determined by a finite-frequency tomography technique (Montelli et al., 2004). Among the eight major Hawaiian Islands, the progressive northwestward movement of the Pacific plate over the plume has resulted in increasing age of islands along the path of motion (Figure 2). Ni'ihau (northwest) is the oldest and the Island of Hawaii (southeast) is the youngest island in the Hawaiian archipelago.

The Island of Hawaii and its submarine base formed from seven independent volcanoes, Mahukona, Kohala, Mauna Kea, Hualalai, Mauna Loa, Kilauea, and Lo'ihi. The five major shield volcanoes are Kohala, Mauna Kea, Hualalai, Mauna Loa, Kilauea (oldest to youngest), while Mahukona lies submerged offshore north of Kailua–Kona and Lo'ihi seamount is beneath the sea (-980 m) to the southeast of Mauna Loa (Sherrod et al., 2007). Mahukona, Kohala, Mauna Kea, and Hualalai have completed their shield-building stages (about 465 ka, 245 ka, 130 ka, and 130 ka, respectively) while Mauna Loa, Kilauea and Loi'hi have not yet completed the shield-building stage. Mauna Loa and Kilauea are currently active in the shield stage and Lo'ihi is in transition between the pre-shield and shield stage (Moore & Clague, 1992). The oldest volcano on the island, Kohala, ceased eruptive activity is about 120 k years ago, the second oldest volcano, Mauna Kea, ceased eruptive activity about 4 k years ago, and the last eruptive event on the youngest of these three volcanoes, Hualälai, occurred in 1800–1801. Mauna Loa and Kilauea have erupted on timescales ranging from every two or three years to tens of years through the past two centuries (Tilling & Heliker, 2010). The Pu'u'O'o eruptive center (Figure 4) along the east rift zone of Kilauea has been in nearly continuous eruption since 1983 (Hekiler et al., 2003).

Lavas erupted by the Hawaiian volcanoes range in chemical composition from alkali-basalt to silica-saturated tholeiites, and there is a systematic change in magma composition associated with the stage of shield building. The earliest alkaline pre-shield stage is followed by the tholeiitic shield stage (more than 95% of the volcanic edifice is built after shield stage), and this is then followed by post-shield stage that produces a thin layer of alkali-basalt and associated differentiated lava on top of the tholeiitic lavas (Clague & Dalrymple, 1987). This systematic shift in magma composition is related to movement of the volcano over the relatively fixed mantle plume. The transition from tholeiitic to alkaline lavas can occur before the end of the shield building stage for large shield volcanoes (summit >4 km), occur after the shield building

stage, or not occur at all for small volcanoes (Moore & Clague, 1992). Pre-shield alkaline lavas can be found at the submarine volcano, Loi'hi. The oldest layers at Kilauea contains alkaline pre-shield lavas (~375 ka) erupted when this volcano was located at the leading edge of the mantle plume. Younger lavas form the entire tholeiitic shield stage (shield-building began at least ~225 ka), and 90% of lava flows on Kilauea are young than 1.5 ka (Sherrod et al., 2007). Mauna Loa has lava flows with similar chemical composition as Kilauea and is at a similar stage of evolution. The main shield-building stage formed by eruption of tholeiites occurs when the volcanoes lies over the center of the plume. Lavas on Mauna Kea record the transition between tholeiitic shield and alkaline post-shield lavas that form when the volcanoes move over the trailing edge of the mantle plume (Sherrod et al., 2007).

Two parallel chains (Kea trend and Loa trend) of Hawaiian volcanoes (Figure 3) are recognized from many geochemical studies (e.g., Abouchami et al., 2005; Hanano et al, 2007; Hofmann & Farnetani, 2013; Frey et al, 2016). The different characteristics that distinguish these two trends can be explained by a concentrically zoned mantle plume model, in which volcanoes on the Kea trend are formed from a peripheral region of the mantle plume, while those on Loa trend are formed from a central region of the mantle plume (Abouchami et al., 2005). An alternative explanation is that the mantle plume has bilateral compositional asymmetry with compositional heterogeneities that are vertically continuous. This latter alternative has been proposed on the basis of lead isotope studies (Abouchami et al., 2005). On the Island of Hawaii, Kohala, Mauna Kea, and Kilauea lie along the Kea trend whereas Māhukona, Hualalai, Mauna Loa, and Lo'ihi Seamount lie along the Loa trend. Differences among the volcanoes on each trend can be identified by studies of trace elements and isotopes (e.g., Hofmann & Farnetani, 2013).

The size of the mantle plume (radius ~300 km) is estimated to be large enough to feed three active volcanoes, Mauna Loa, Kilauea, and Lo'ihi, (and possibly also Hualalai and Haleakala), and the pathways that feed magma to each volcano are much narrower than the plume (Tilling & Heliker, 2010). Although fed from the same deep source, Mauna Loa and Mauna Kea probably have their own shallow magma reservoir systems that are independent of each other (Tilling & Heliker, 2010). In contrast to the vertical extent of the mantle plume ≥2350 km, the crustal thickness beneath Hawaiian volcanoes is very small, estimated as ~12 km under Kilauea, ~18 under the center of Maui, and ~21 km under Oahu (southeast to northwest) from seismic studies (Furumoto et al., 1968).

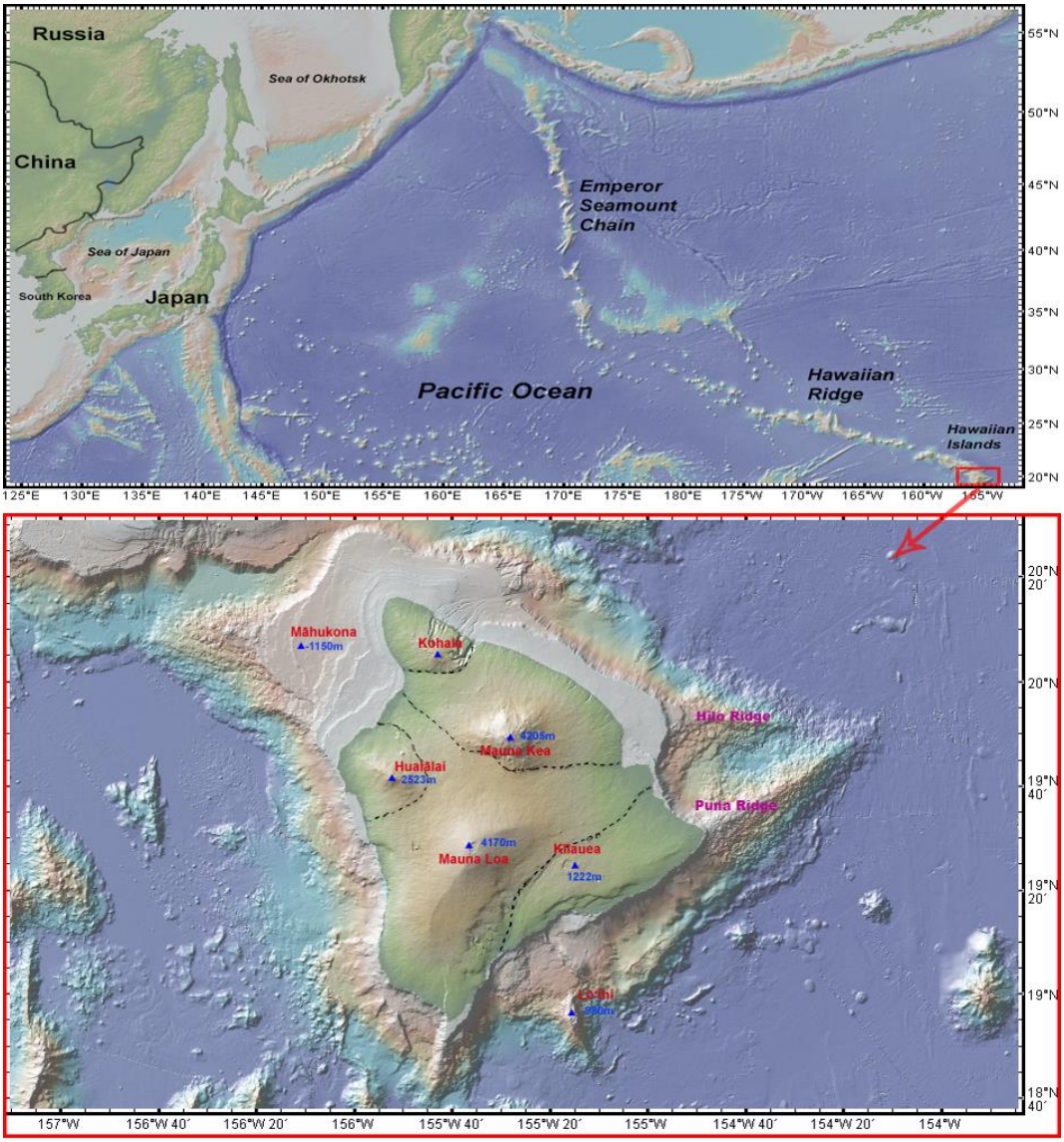

Figure 1. Topographic map of the Big Island of Hawaii that is located at the southeastern end of the the Hawaiian Emporer Seamount Chain in the Central Pacific. The Big Island is the youngest and biggest among the eaight major islands in the Hawaiian archipelago. On the Island, five major shield volcanoes include Kohala, Mauna Kea, Hualālai, Mauna Loa, and Kilauea. A sixth volcano, Māhukona, lies offshore north of Kailua–Kona. A seventh volcano, Lō'ihi Seamount, is the newest one and lies 980 m below sea level. The submarine extension of shield volcanoes, Puna Ridge and Hilo Ridge, are marked in magenta. Generated by GeoMapApp.

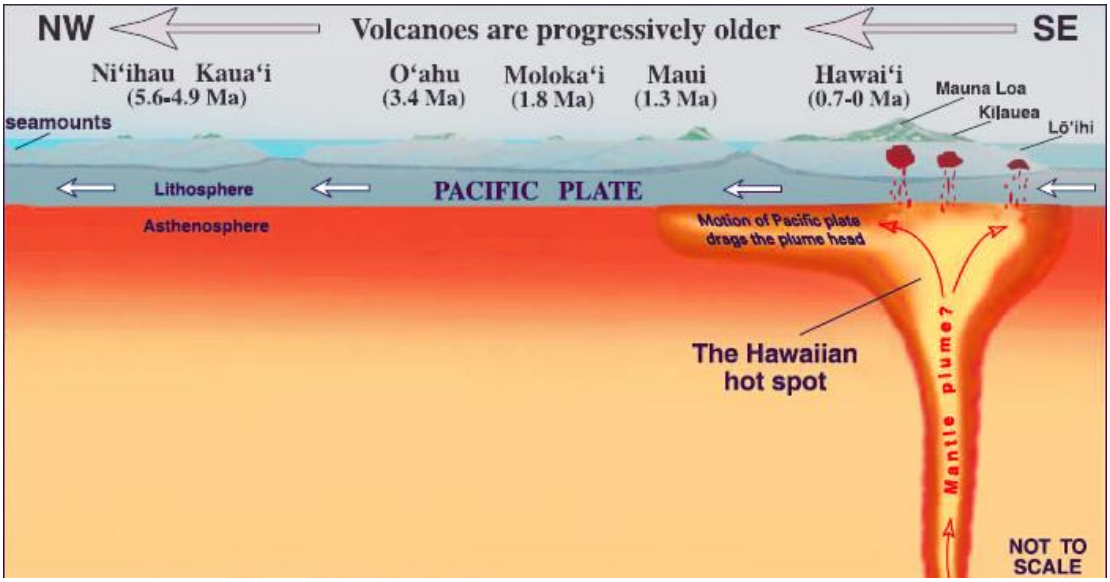

Figure 2. The eight major islands in Hawaiian island chain fed by the inferred mantle plume below the overriding Pacific Plate. The geologic ages of the oldest volcano on each island are progressively older to the northwest as a result of motion of Pacific Plate over the hot spot. "Ma" is millions of years ago. From Tilling & Heliker (2010). Modified from image of Joel E. Robinson, USGS, in "This dynamic planet" (Simkin et al, 2006).

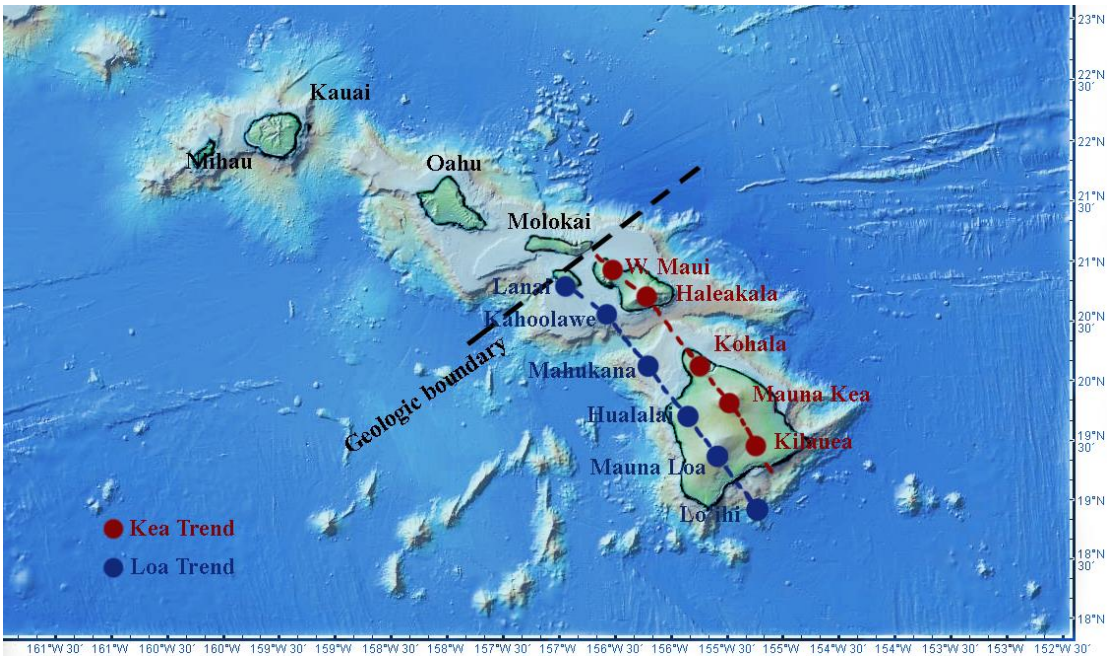

Figure 3. Topographic map of the eight major Hawaiian islands, showing the Kea and Loa trends. On the Big Island of Hawaii (southest), Kohala, Mauna Kea, and Kilauea belong to the Kea trend, while Mahukana, Hualalai, Mauna Loa, and Lo'ihi belong to the Loa trend. The position of two trends and "geologic boundary" according to interpretations in Abouchami et al. (2005). Generated by GeoMapApp.

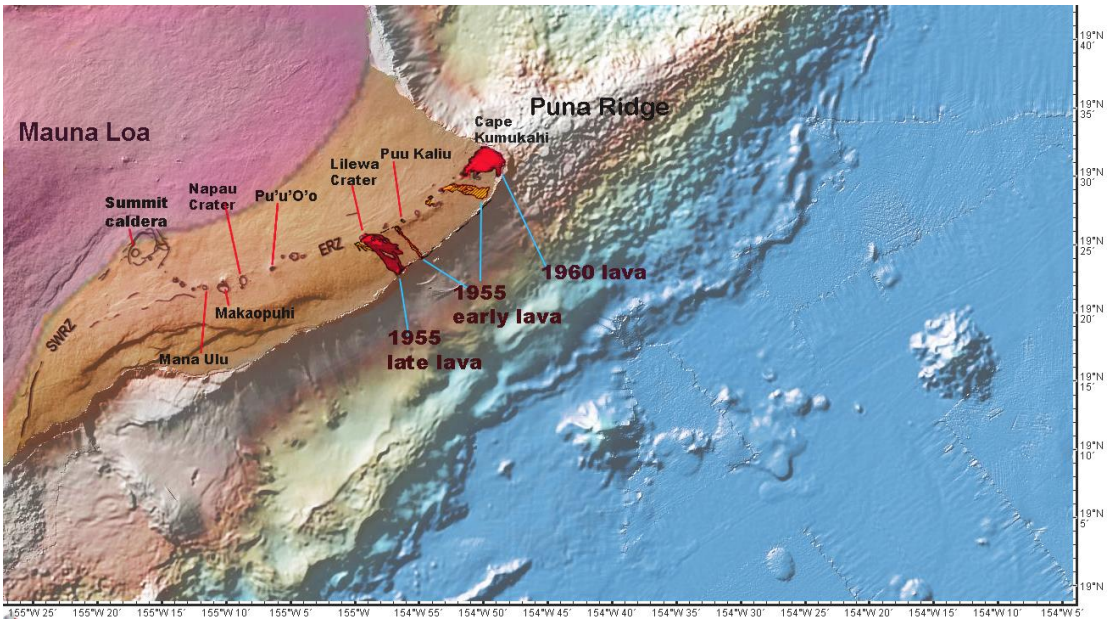

Figure 4. Topographic map of Kilauea on the Island of Hawaii, showing eruptive centers on the east rift zone. SWRZ is southwest rift zone, and ERZ is east ridt zone. The pressure (and depth) of samples of summit caldera, Makaopuhi, Pu'u'O'o, ERZ 1955 late, ERZ 1960 early, ERZ 1960 late, ERZ 1960 undivided, and Puna ridge (listed in Table 2; also seen in Figure 22 & Figure 23) are studied in this research. The location of 1955 and 1960 lavas are according to the illustrations in Wright & Helz (1996). Generated by GeoMapApp.

METHODS

Determining Pressure of Crystallization

The depth of magma chambers beneath the volcanoes can be estimated by calculating the pressure of partial crystallization, the pressure at which crystallization begins prior to eruption. This can be done because depth (z) has a positive correlation with pressure (P). The pressure (P) and hence depth (z) of partial crystallization of magma can be estimated by variety of petrologic techniques. In this study, the method that is used to calculate the pressure is a quantitative petrologic method based on chemical compositions analyses of glasses described by Kelly & Barton (2008).

With a large number of samples, the most appropriate method to determine the pressure is based on a comparison of the compositions of natural samples of basalt with the compositions of liquids lying along the pressure-dependent olivine (ol), plagioclase (plag), and clinopyroxene (cpx) cotectic boundary. Many basaltic melts crystallize these three minerals, and therefore this method is appropriate for use with a large number of basalt samples, and relies on the experimentally verified observation that the position of the cotectic dependent on pressure (eg. Yang et al. 1996). In order to illustrate the method graphically, it is necessary to reduce the ten-dimensional system of 10 major components necessary to describe the compositions of basalt to a smaller number of components, and this is done by recalculation the components into the four components CaO-MgO-Al_2O_3-SiO_2.With the chemical compositions converted into normative mineral components, compositions can be plotted in the basalt tetrahedron formed by four major normative minerals (Figure 5a). Compositions can then be projected from one of the mineral components onto ternary planes that can be treated as pseudoternary phase diagrams for the purpose of observing the phase relations between liquids and certain minerals. If the phase relationships are projected from plag onto the ol-cpx-qtz pseudoternary plane using the recalculation procedure of Walker et al. (1979), the effect of pressure on the cotectic liquid composition on the pseudoternary phase plane can be illustrated (Figure 5b). In this figure, the positions of ol-plag-cpx cotectic shift toward olivine with increasing P. Similarly, projection of phase relationships from ol onto the plag-cpx-qtz pseudoternary plane shows that the plag-cpx-qtz cotectic shifts towards plag with increasing P. Because the cotectic shifts toward ol and plag on the pseudoternary planes ol-cpx-qtz and plag-cpx-qtz, respectively, the cotectic shifts away from cpx, which means that higher pressure favors earlier crystallization of cpx resulting in development of a trend of decreasing CaO with decreasing MgO in liquids at an earlier stage of crystallization.

Based on these phase relationships, mathematical models can be developed to describe quantitatively how melt compositions change systematically with pressure. Yang et al. (1996) gave three equations that describe the liquid composition along the ol-plag-cpx cotectic as a function of pressure (P) and temperature (T). They used these equations and a graphical method to find the pressure of crystallization of basalt compositions. Kelly & Barton (2008) solved the equations of Yang et al. (1996) to calculate the pressure based on projections from plag onto the ol-cpx-qtz plane and from ol onto the plag-cpx-qtz plane, with the liquid compositions converted to normative mineral components. These projections were chosen because most basalt melts are saturated with ol and plag. As a result, six values of P for each sample are calculated, three from ol, cpx and qtz in the plag projection and another three from plag, cpx and qtz in the ol projection. The average of these six values of P gives the pressure of partial crystallization and

the standard deviation of all six values gives the uncertainty in the calculated pressure. This method is preferable to graphical methods because the mathematical approach allows rapid calculation of pressures for each sample in large data sets.

The calculations are done using the Microsoft Excel program described by Kelley and Barton (2008). The major oxide compositions of basaltic glasses are compiled as input data and put into the three equations of the mathematical model. Analyses of glasses are used rather than the whole rock analyses because glasses represent samples of quenched melts, or pre-eruptive liquid compositions, while whole-rock samples could represent mixtures of crystals and melts (Kelly & Barton, 2008). Rather than representing a composition formed in a closed system, whole-rock compositions could have been affected by the accumulation of crystals or incorporation of xenocrysts. Hence, use of whole-rock analyses as the melt compositions and using it as the input data could generate results with large errors of pressure.

Uncertainty

The accuracy of the calculated pressure can be determined by comparing the pressures calculated from glass analyses representing liquids produced in experiments with the recorded pressures of those experiments. Despite the inherent errors in experimental results caused by factors such as the effects of unknown amounts of volatiles in nominally anhydrous experiments (Kelly & Barton, 2008), the difference between the pressure obtained from calculations and those of the experiments can be considered as the difference between the calculated and the actual values of pressure of partial crystallization. The accuracy of this method is within ± 126 MPa (1σ). In comparison to the method described by Michael & Cornell (1998) that is based on one rather than all three of the equations of Yang et al. (1996), the Kelly & Barton method employed herein is more accurate, because pressures calculated with the Michael & Cornell method are accurate to ± 160 MPa (1σ) for the same set of samples.

Converting Pressure to Depth

The corresponding depth (z) of samples can be determined with the equation:

$$\mathbf{P = \rho * g * z}$$

where ρ represents density of the crust. In this case, a value of 2900 kg/m^3, appropriate for the density of middle or lower crust below the ocean can be considered as the average density of oceanic crust for Hawaiian Islands. An average value of 9.8m/s^2 is used for g, the acceleration due to gravity.

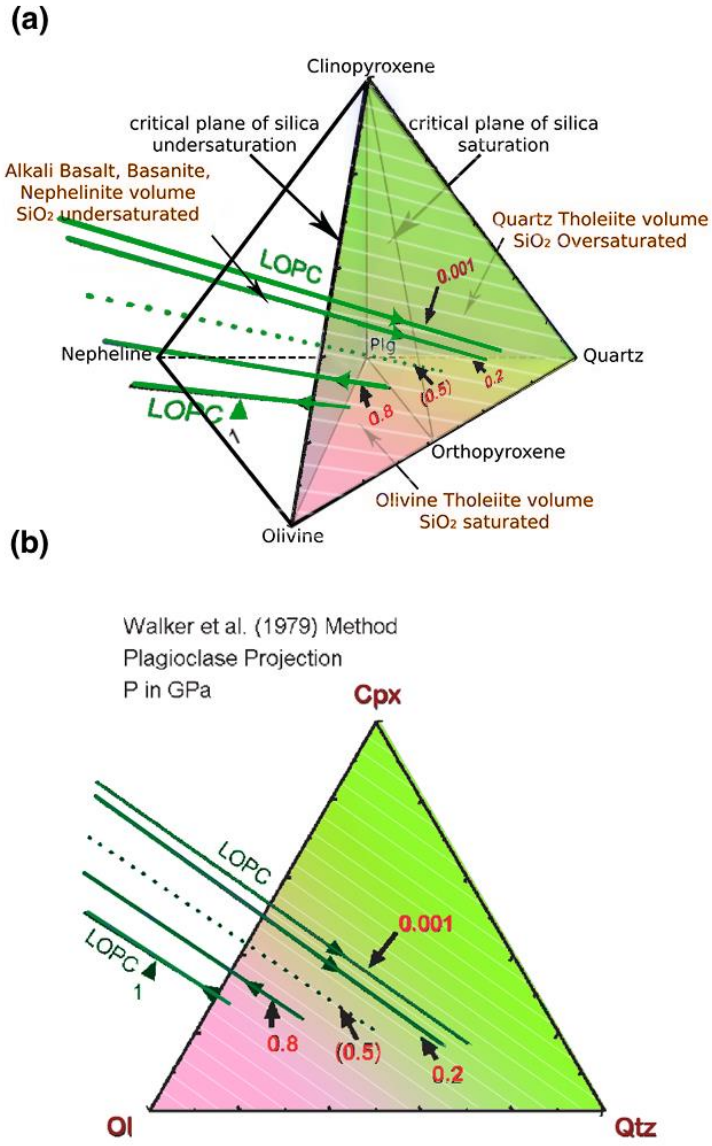

Figure 5. **(a)** Basalt tetrahedron with four major normative mineral components: Olivine (ol), Clinopyroxene (cpx), Napheline and Quartz (qtz) (after Yoder & Tilley, 1962). The point marked "Plg" on the nepheline-quartz edge represents Plagioclase. Kelly & Barton method used the four-dimensional system of CaO-MgO-Al_2O_3-SiO_2, which can be converted to normative mineral components *cpx-ol-plag-qtz* (represented by the tetrahedron with vertexes *cpx, ol, plag,* and *qtz*). From one corner the phase relationships can be projected onto the pseudoternary phase diagrams of three other minerals. **(b)** The phase relationships from *plag* are projected onto the ol-cpx-qtz pseudoternary plane using the recalculation procedure of Walker et al (1979) from the *cpx-ol-plag-qtz* tetrahedron in Figure 5a. The shift of LOPC (Liquid-olivine-plagioclase-Clinopyroxene cotectic) shows the effect of pressure on the liquid composition on *ol-cpx-qtz* pseudoternary phase plane. LOPC shifts toward *ol* with increasing pressure. (*The another projection from *ol* onto *plag-cpx-qtz* plane can be done in the same way and on that pseudoternary phase plane the liquid line of decent will shift towards *plag* with increasing pressure.) Modified from Kelly & Barton (2008).

SAMPLES

The analyses used for calculation of pressure were compiled from published and unpublished glass analyses. Sources of analyses include 21 publications in scientific journals and one unpublished source (Table 1). The database includes >2000 glass analyses from samples collected from the four active volcanoes, Kilauea, Mauna Kea, Mauna Loa, and Lo'ihi seamount. Each analysis contained data for 10 major oxides that are common components in basalt (SiO_2, Al_2O_3, TiO_2, FeOT, MnO, MgO, CaO, Na_2O, K_2O, and P_2O_5) recorded in weight percent (wt %). After removal of samples with incomplete analyses of major oxides (with the exception of MnO which was set to 0 wt % if MnO was not analyzed) and removal of the duplicate analyses after the datasets were combined and sorted by different localities, the total number of analysis that were used as input data was 1576. The analytical instrument for determining the major element abundance of glasses from each volcano is the electron microprobe. This instrument cannot quantitatively distinguish between FeO and Fe_2O_3, and the total Fe content is reported as FeO. Any Fe_2O_3 reported in an analysis was converted to FeO.

Kilauea and its submarine extension, the Puna Ridge, had the largest dataset and included samples from a wide range locations including the summit, Pu'u'O'o, the Puna Ridge and other locations on the east rift zone (Table 2). A large proportion of the samples in the dataset for Mauna Kea were collected by Hawaii Scientific Drilling project (HSDP) which drilled a 1.1 km hole at the east flank of Mauna Kea (Yang et al, 1994, Stolper et al., 2004). The samples from the HSDP2 drill hole that passed through submarine deposits include four rock types, hyaloclastites, massive basalts, pillow basalts, and intrusives (Stolper et al., 2004). The samples in the Mauna Loa dataset comprise submarine glasses, subaerial glasses, and olivine-hosted glass inclusions, Submarine glasses were collected from dredge hauls on the western flank and southwest rift zone (Davis et al, 2003). Lo'ihi has the smallest dataset, in which a large number of samples were collected from the southern cone on the southeast summit plateau. The samples include lapilli matrix glasses, ash matrix glasses and olivine-hosted glass inclusion, (Schipper et al., 2011). Some samples of tholeiite glasses from glass-rich pillow fragments, were collected by Scripps Institution of Oceanography Benthic Expedition in 1982 in four dredges (Hawkins & Melchior, 1983). At each of the four volcanoes, some of the samples are fresh, unaltered tholeiitic pillow-rim glasses obtained from dredges of deep submarine extensions of the rift zones of these volcanoes (1900–3700 m) by a 1983 R/V KANA KEIKI cruise (Garcia et al, 1989).

The 1576 samples used as input data are sorted by locations as Kilauea without Puna Ridge (subaerial), Puna Ridge, Mauna Kea and Mauna Loa (Table 1). Kilauea samples with recorded information about the eruptive center and year of eruption are sorted by time and location (Table 2). Compositional data for samples from each location are summarized in Table 3. Based on the TAS classification scheme (wt.% SiO_2 versus Na_2O+K_2O), 1347 out of 1567 samples are classified as basalts, while the remaining samples are basaltic andesites, andesite (SiO_2 >52%), or tephrite basanites (SiO_2<45%, Na_2O+K_2O>5%). The distribution of samples from Kiluaea, the Puna Ridge, Mauna Kea, Mauna Loa, and Lo'ihi are shown on the TAS classification scheme in Figure 6, and the distribution of samples collected from various location on Kilauea is shown in Figure 7.

Most of the non-basaltic samples are basaltic andesite but a few samples are classified as andesite and tephrite basanite. The non-basaltic samples from subaerial locations on Kilauea and Mauna Loa contain both basaltic andesite and andesite. The number of basaltic andesite samples is 36 of 552 for Kilauea and 157 of 287 for Mauna Loa, whereas the number of andesites for each locations is only 1. For samples collected from the subaerial parts of Kilauea, those from the East Rift Zone and summit are all basalt, whereas the samples from Pu'u'O'o include some basaltic andesites (29 of 312). The non-basaltic samples from the Puna Ridge (5 of 40) and Mauna Kea (17 of 579) are all basaltic andesites. Note that the proportion of basaltic andesite samples is much greater for Mauna Loa than for the other localities.

The composition of samples of Loi'hi differs from composition of samples from the other locations. The non-basaltic samples (3 of 118) from Loi'hi are all tephrite basanite and contain higher total Na_2O+K_2O and lower SiO_2 than basalt. Also, in contrast to the other locations, samples from Loi'hi defined as basalt have a narrower and lower range of SiO_2 and a wider and higher range of Na_2O+K_2O (Figure 6). The SiO_2 contents of basaltic samples from Loi'hi fall in the range of 45–51 wt. %, while of the range for samples from all other locations is 47–52 wt. %. The range of Na_2O+K_2O for basalt samples from Loi'hi is 2–5 wt. %, while the range for samples from other locations is 2–4 wt. %. According to the criterion proposed by Macdonald (1968) for Hawaiian lavas, most samples from the Big Island of Hawaii are tholeiitic (sub-alkaline). With the exception of one sample from the Puna Ridge, all samples from Kilauea and Mauna Loa are sub-alkaline, as expected from the conclusions of previous workers that surface lava flows from Mauna Loa and Kilauea are tholeiites (e.g., Sherrod et al., 2007). Two samples from Mauna Kea are alkaline but the remaining samples are sub-alkaline and can be classified as tholeiites. The abundance of tholeiites on these volcanoes is consistent with eruptions defining the shield stage. Loi'hi is the only location with a relatively large number of alkaline samples (47 of 118), including both alkali-basalts and tephrite basanites. These samples have the characteristics that define eruptions in the pre-shield stage. Many of the Lo'ihi samples have compositions that straddle the boundary between alkaline and sub-alkaline magmas and can be considered as transitional compositions erupted between the pre-shield and shield stages of volcano growth.

Table 1. Number of samples from each volcano on Big Island of Hawaii that are compiled from publications and used as input data (also the number of results without filtration of each volcano). The samples from Puna Ridge are separated from the subaerial area of Kilauea. The sources are shown in the last column.

Volcanoes	Location/Eruptive Center	Number of Samples	Sources
Kilauea	Total	592	Clague et al. (1995). Clague, D.A., unpublished. Garcia et al (1989). Helz & Wright (1992). Moore & Krivoy (1964). Murata & Richter (1966). Nicholls & Stout. (1988). Peck et al (1966). Thornber (2001). Wright & Helz (1996). Wright & Okamura (1977).
	*Total Samples without Puna Ridge (Subaerial)	552	
	Puna Ridge	40	Clague et al. (1995).
Mauna Kea		579	Clague, D.A., unpublished. Garcia et al. (1989). Stolper et al. (2004). Yang et al. (1994).
Mauna Loa		287	Clague, D.A., unpublished. Davis et al. (2003). Garcia et al. (1989). Rhodes (1995).
Loi'hi		118	Clague, D.A., unpublished. Garcia et al. (1989). Hawkins & Melchior (1983). Moore et al. (1982). Schippers et al. (2011)
Total		1576	

Table 2. Number of samples from each area or eruption center of Kilauea Volcano. The samples are sorted based on eruptive centers/areas and year of eruption. The sources are shown in the last column.

Location/Eruptive Center	Number of Samples	Sources
*Kilauea Total Samples	592	Same as listed in Table 1.
*Total Samples without Puna Ridge (Subaerial)	552	
Puna Ridge	40	Clague et al. (1995).
Summit (Halema'uma'u Crater and Haiika Crater 1967-1968; 1959 Summit Eruption)	7	Nicholls & Stout (1988).
Makaopuhi lava lake	10	Wright & Okamura (1977).
Pu'u'o'o (1994-1998)	312	Thornber (2001).
East Rift Zone (1955 late)	5	Helz & Wright (1992).
*East Rift Zone (1960)	22	Murata & Richter (1966). Wright & Helz (1996).
East Rift Zone (1960 early)	6	Wright & Helz (1996).
East Rift Zone (1960 late)	12	Wright & Helz (1996).
East Rift Zone (1960 undivided)	4	Murata & Richter (1966).

Table 3. Number of each magma type for different locations. Magma types are determined based on chemical characteristics (wt. % of total alkali vs SiO2). Basaltic samples are defined as SiO2 wt. % ≤45% and ≥52%, and Na2O+K2O wt. % ≤5%). Any samples with SiO2 wt. % >52% or <45%, and Na2O+K2O wt. % >5%) are non-basaltic. In this case, non-basaltic samples include basaltic andesite, andesite, and tephrite basanite. The non-basaltic samples will be removed during data filtration, as Kelly & Barton method is calibrated only for basalt. Those cells marked by diagonal up border means they have no samples of a certainty magma type.

Volcanoes	Location/ Eruptive Center	Total Number of Samples	Basaltic Andesite	Andesite	Tephrite Basanite	Total Non-basaltic	Total Basalt
Kilauea	Total	592	41	1		42	550
	*Total Samples without Puna	552	36	1		37	515
	Puna Ridge	40	5			5	35
	East Rift Zone (1955 and 1960)	27					27
	Summit	7					7
	Pu'u'o'o	312	29			29	283
Mauna Kea		579	17			17	562
Mauna Loa		287	157	1		158	129
Loi'hi		118			3	3	115
Total		1567	215	2	3	220	1347

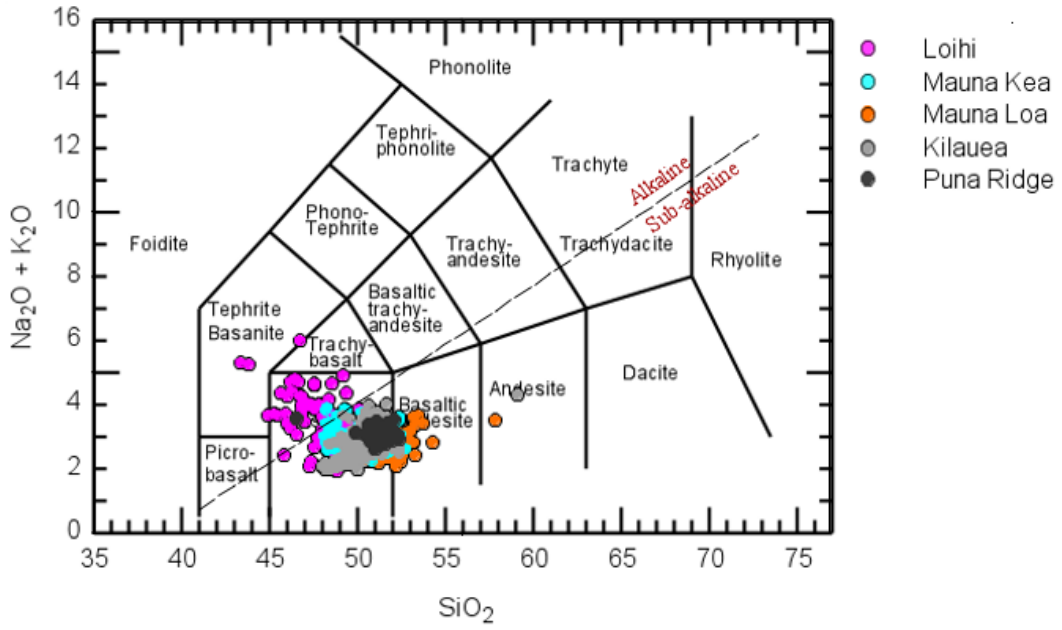

Figure 6. Total Alkali Silica (TAS) diagram that shows the compositional analyses of Na_2O+K_2O versus SiO_2 (wt. %) for glasses from 5 locations, Kilauea without Puna Ridge (grey), Puna Ridge (black), Lo'ihi (magenta), Mauna Kea (cyan), and Mauna Loa (orange), on the Big Island of Hawaii. The boundaries between magma types are from Le Bas et al. (1986). The box with SiO_2 wt. % ≤45% and ≥52% and Na_2O+K_2O wt. % ≤5% where most of the samples covered on is labeled as "basalt". Only basaltic samples can be used for pressure calculation, because the method of Kelly & Barton (2008) is calibrated only for basalt. The dash line represents the boundary between sub-alkaline or tholeiitic and alkaline compositions proposed by Macdonald (1968) for Hawaiian lavas.

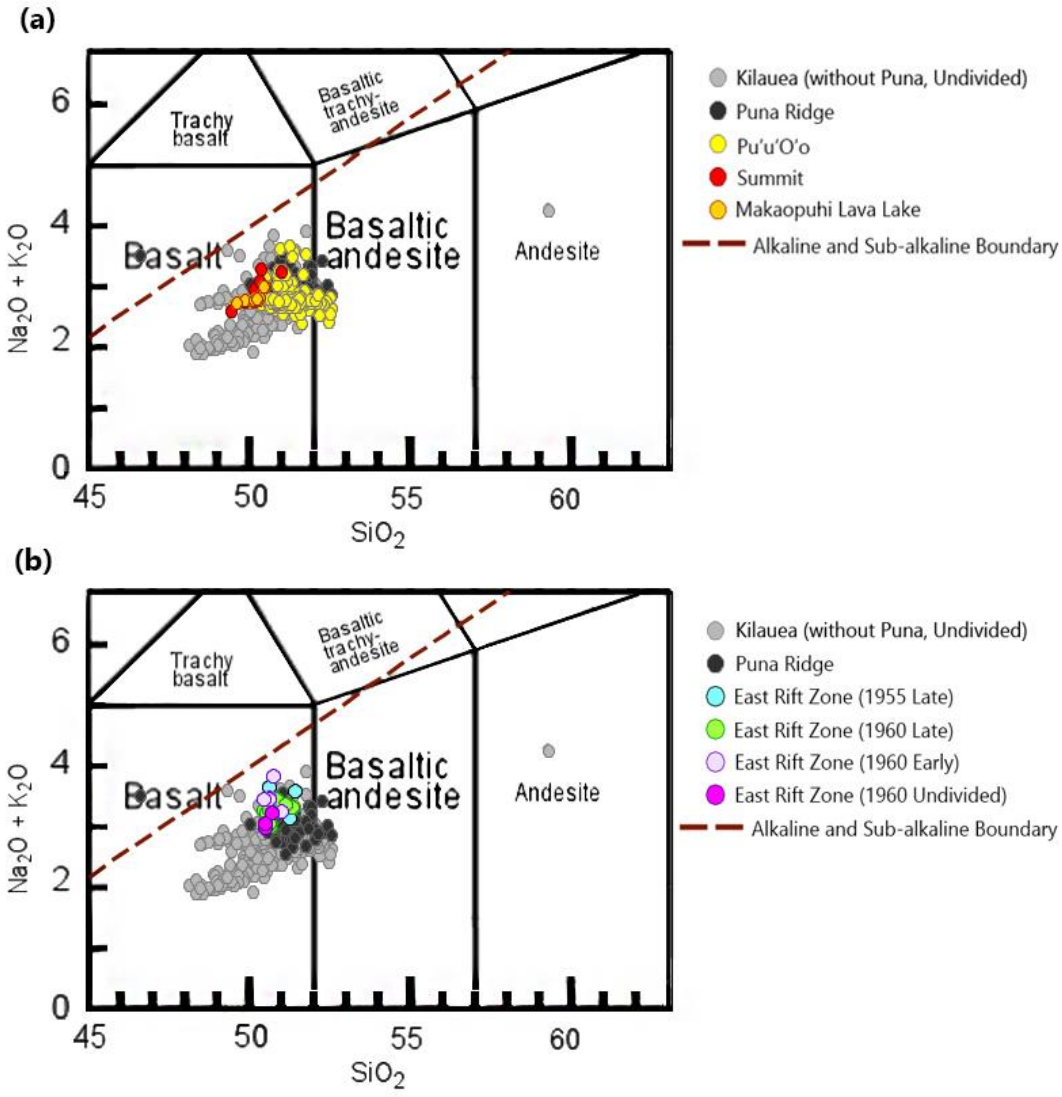

Figure 7. Na_2O+K_2O versus SiO_2 (wt. %) content of samples from Kilauea and its submarine extension (Puna Ridge). The compositional analyses for different eruptive centers and areas of Kilauea are marked by different colors and shown on the magnified Total Alkali Silica (TAS) diagrams. The boundaries between magma types are from Le Bas et al. (1986). Basalt is defined by SiO_2 wt. % ≤45% and ≥52% and Na_2O+K_2O wt. % ≤5%. The dash line represents the boundary between sub-alkaline or tholeiitic and alkaline compositions proposed by Macdonald (1968) for Hawaiian lavas. **(a)** Compared samples from summit area, Makaopuhi, and Pu'u'O'o with those undivided subaerial Kilauea and Puna Ridge samples. **(b)** Compared samples from different areas at the East Rift Zone with those undivided subaerial Kilauea and Puna Ridge samples.

RESULTS

Pressures of partial crystallization were calculated for all glasses from each location. Without data filtration by the various criteria described in the following section of this work, the unfiltered results could include pressures that are unrealistic or unreliable and such results should not be used for interpretation of magma reservoir depths. Nevertheless, it is important to describe the unfiltered results because these reflect the compositional characteristics of the original glass dataset for each location included in this study. The unfiltered results provide the context and rationale for the filtering process described in the following section.

The unfiltered results are shown in Figure 8 on plots of calculated pressure versus MgO content of the glasses. There is a large number of samples (552 samples for Kilauea without Puna Ridge and 118 samples for Lo'ihi) for each location. Therefore, these results provide a general overview of the pressures obtained over the whole area of each locality, and provide insight into the distinct characteristics of the data distribution (e.g., high versus low MgO, high versus low pressure) for each locality. The calculated pressures for the 552 Kilauea samples (without its east submarine extension, Puna Ridge) fall in range of -271 to 875 MPa. A narrower range of pressures is obtained for samples from the Puna Ridge, (-163 to 562 MPa) and for Mauna Kea (-242 to 524 MPa) than for subaerial Kilauea lavas. Calculated pressures for glasses from Mauna Loa also show a range of values (-437 to 355 MPa), although the highest and lowest pressure obtained for these samples is lower than that obtained for glasses from Kilauea, the Puna Ridge and Mauna Kea. Lo'ihi is the only location with an extremely large range of pressures, as the highest pressure is 1414 MPa and, if the one outlier that yields a pressure of 2211 MPa is ignored, the lowest limit of pressure is -459 MPa.

The grey lines that mark the pressure 0 MPa and increments of 500 MPa for each graph (Figure 8) are drawn to compare the range of pressures obtained for samples from the different localities. It can be seen that many samples cluster near the pressure at the surface (taken as 0.1 MPa in this study) at each location. Also there are samples from all localities that yield negative values of calculated pressure. If we neglect the one outlier from Lo'ihi that yields an anomalously low pressure of -2211 MPa, the values of negative pressure calculated for samples from all locations range inform 0 MPa to -459 MPa. The negative pressures are unrealistic results. However, because the uncertainty of pressures calculated for each sample is ±126 MPa, negative pressures between 0.1 and -126 MPa can be considered to represent crystallization at 0 MPa, taken as the pressure at the surface (see the discussion in the "Data Filtration" Section). For interpretation of the results, therefore, negative pressures between 0.1 and -126 MPa are considered to represent actual pressures of partial crystallization at 0.1 MPa and these results are taken to be acceptable for interpretation of the magma plumbing systems beneath Hawaiian volcanoes.

About 45% of the total number pf pressures calculated for all samples (705 out of 1567) are negative values (Table 4). However, 662 of these negative pressures are between 0.1 and -126 MPa, or about 39.740% of the total results. Therefore, the pressures calculated for these 662 samples are within uncertainty of 0.1 MPa and these results are considered acceptable results. This means that only 5.3% of total results are more negative than -126 MPa and so are considered as unacceptable results. The percentage (39.4%) of negative results for samples from Kilauea (including Puna Ridge) is similar to that for all samples. The percentage of negative results for Mauna Kea and Mauna Loa is larger than that for all samples (51.1% and 55.7%, respectively), whereas the percentage of negative results for Loi'hi is much smaller (only 13.6%) than that for all samples. For each locality, the percentage of negative results in the range 0 to

-126 MPa is very close to the total percentage of negative results, indicating that the number of samples that yield unacceptable (negative) results is relatively small.

Plots of pressure versus the MgO content of the glasses are shown in Figure 8. If the results for samples that yield unrealistic pressures (negative pressure less than -126 MPa), are disregarded, the data for samples from Kilauea (without Puna Ridge) and Mauna Kea form two distinct groups. For samples with high MgO contents, there is a positive correlation between pressure and MgO (marked by pink arrow) whereas for samples with low MgO contents no correlation between pressure and MgO is apparent (marked by red arrow in Figure 8). In the case of Mauna Loa, there is a rough positive correlation between pressure and MgO from Mauna Loa for high MgO samples, whereas there are no high MgO samples for Puna ridge. For both Maua Loa and Puna ridge there is no correlation between pressure and MgO for samples with low MgO contents. Lack of correlation between pressure and MgO is also seen in many of the results obtained for glasses from Iceland using the same method of calculation (Kelly & Barton, 2008) and also using a different petrologic method to calculate pressure (the method described by Herzberg, 2004). The results for glasses from Loi'hi also form two groups. For samples with high MgO contents, there is a positive correlation between pressure and MgO, but for samples with low MgO contents there is a negative correlation between pressure and MgO. This unusual negative correlation has also been observed for samples from Iceland, and has been attributed to the effects of crustal assimilation (Kelly & Barton, 2008). However, there is no convincing petrographic evidence to support this interpretation for Lo'ihi. As the number of samples available for Kilauea, Mauna Kea, and Mauna Loa greatly exceeds that for Lo'ihi (Tables 1 and 3), a possible explanation is that the apparent negative correlation between pressure and MgO is an artifact of the relatively small sample population, and that a larger dataset containing additional samples collected from Lo'ihi would show a similar relationship between pressure and MgO as the glasses from other volcanoes on the Big Island of Hawaii.

From the unfiltered results plotted in Figure 8, it can be seen that the threshold between these two different relationships of samples, one for samples with high MgO content and one for those with low MgO content, is approximately 7 wt.% of MgO. Plots of compositional data for the glasses on variation diagrams showing the relationship of CaO versus MgO, Al_2O_3 versus MgO, and CaO/Al_2O_3 versus MgO show an inflection at about this value of MgO, and this inflection or change in slope of the data arrays is interpreted to indicate a change in the crystallizing mineral assemblage. The variations for glasses with MgO greater than ~7wt.% reflect crystallization of ol, whereas the variations for glasses with MgO less than ~7wt.% reflect crystallization of ol-plag-cpx. The exact MgO content at which this inflection occurs for each location can be determined from regression analyses of the analyses (see Discussion Section).

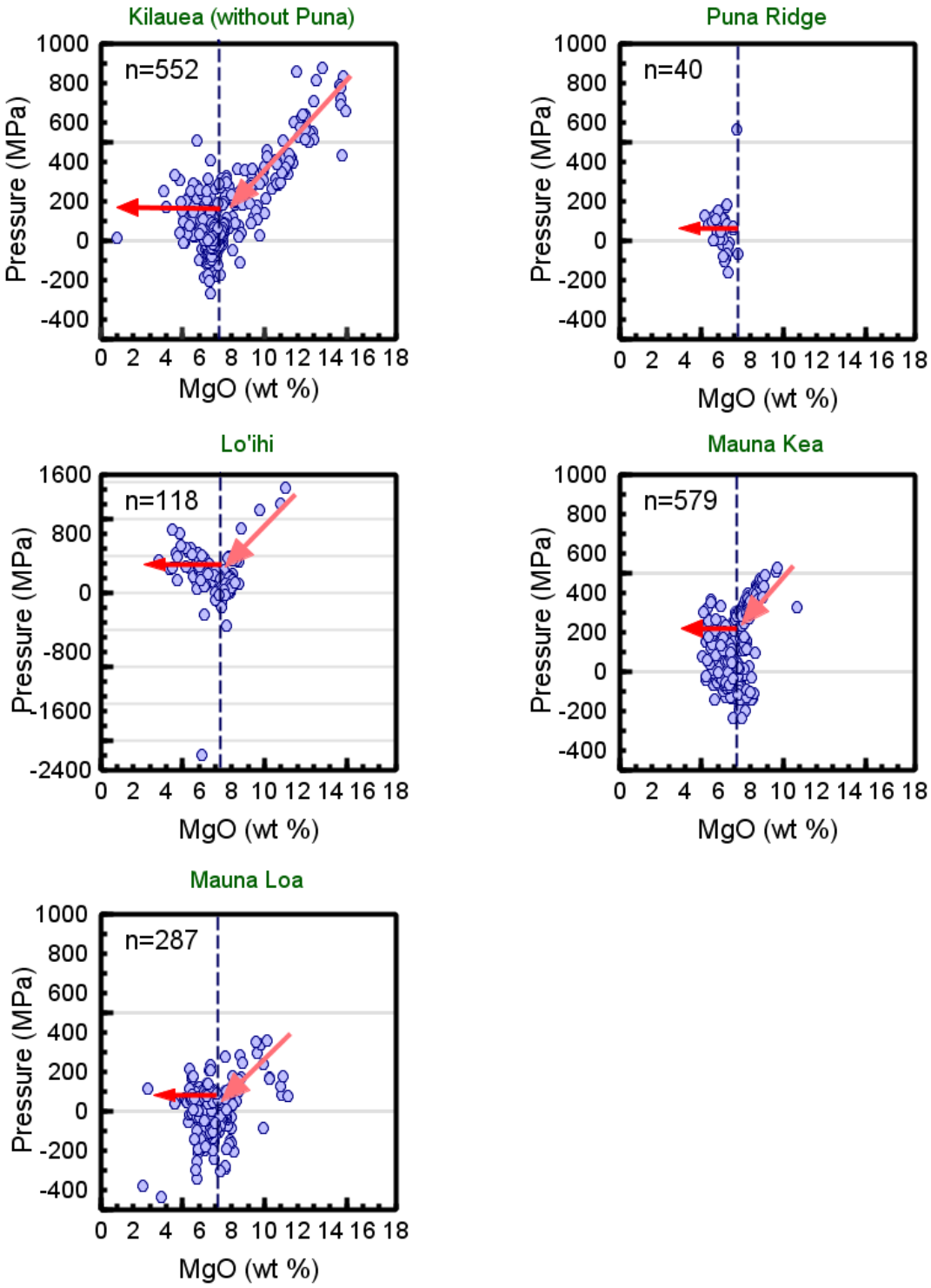

Figure 8. Variation diagrams of pressure vs MgO, showing unfiltered results of calculated pressures for five locations. The grey solid line marked the pressure of with each 500 MPa from 0 MPa. The dark blue dashed line marked the turning point of an MgO wt. % where the relationship between P and MgO of samples change (regardless of negative pressures). The two groups of samples marked by arrows show samples that crystallization *ol±plag* (pink arrow) and those that crystallize *ol-plag-cpx* (red arrow), respectively.

Table 4. Number and percentage of results that yielded negative pressure for each location are shown. 126 MPa is the uncertainty of the calculation of this method. Negative pressures are considered to be unrealistic and not appropriate to be used for data interpretation. However, those results of pressure between 0 to 126 MPa are within the uncertainty of calculation, and will be corrected to 0.1 MPa and still kept in the dataset of results in Data Filtration (Discussion Section).

Volcanoes	Location/ Eruptive Center	Total # of Samples	Number of Total Negative Pressure	% of Total Negative Pressure	Number of negative Pressure (< -126MPa)	% of negative Pressure (< -126MPa)
Kilauea	Total	592	233	39.4 %	224	37.8 %
	*Without Puna	552	221	40.0 %	213	38.6 %
	Puna Ridge	40	12	30 %	11	27.5 %
Mauna Kea		579	296	51.1 %	269	46.5 %
Mauna Loa		287	160	55.7 %	118	41.1 %
Loi'hi		118	16	13.6 %	11	9.3 %
Total		1567	705	45.0 %	662	39.7 %

DISCUSSION

Data Filtration

Pressures of partial crystallization were calculated for a total of 1576 glass analyses using the method described by Kelly & Barton (2008). However, some of the calculated pressures are unrealistic, some are unreliable, and some of the results are calculated for glasses with compositions that are not appropriate for use with this method. Accordingly, it is necessary to filter the results to exclude results that are unrealistic, unreliable or inappropriate. The methods used to filter the results are described below, and are based on criteria based on evaluation of errors associated with calculation of the pressures, on consideration of magma compositions, and on analysis of chemical variations.

The method used to calculate the pressures of partial crystallization is calibrated only for basalt compositions. The first step in filtering was to filter results for all non-basaltic samples (SiO_2 wt. % >52% or <45%, and Na_2O+K_2O wt. % >5%) out of the datasets. As a result, total 220 (out of 1567) non-basaltic samples were removed leaving 1347 basaltic samples (Table 3). The number of samples from Mauna Loa is substantially reduced in this step, as more than half of the samples (158 out of 287) were removed.

The second criterion used to filter the results is based on the observation described in the preceding section that some samples yield negative pressures (Figure 8) and these are clearly unrealistic results. However, the accuracy of calculated pressures is ±126 MPa (Kelley and Barton, 2008), and therefore, pressures of -126 MPa could, in principle, be calculated for samples that crystallized at an actual pressure of 0.1 MPa (at the surface). For this reason, samples that yielded negative pressures more than -126 MPa (e.g., -200 MPa) were removed from the dataset, whereas those in the range of -126 to 0 MPa that possibly represent the pressure of crystallization at the surface were converted to 0.1 MPa taken as the value of atmospheric pressure at the Earth's surface (1 atm). After this filtration, 5.3 % of negative results are removed while 39.7% (-126 to 0 MPa) are corrected to 0.1 MPa (Table 4). Therefore, a potential effect of this process is that the average pressure calculated using the filtered results for each location could be dominated by results for a large number of samples taken as 0.1 MPa (e.g., 46.5% of samples from Mauna Kea corrected as 0.1 MPa), even though in reality corrected pressures could reflect any value between 0.1 and 126 MPa.

The third criterion of data filtration is based on the uncertainty associated with the value of pressure calculated for each sample. As described in the section on methods, the uncertainty associated with pressures calculated with the Kelley-Barton method is ±126 MPa (1σ). Calculated pressures with an uncertainty (1σ) greater than ±126 MPa are considered to be unreliable and were filtered from the results. As discussed by Kelley and Barton (2008), a calculated pressure associated with a large uncertainty indicates that the glass composition does not correspond to that of a liquid lying on the ol-plag-cpx cotectic, and therefore the composition is not appropriate for calculating pressure using this petrologic method.

Using this criterion for data filtration, 9.1% of results are filtered out from the original dataset (Table 5). The dataset from Loi'hi has the most results (35.6%) with a high uncertainty among all datasets and these results were removed. As a result, all of the results for individual samples after this filtration have errors between 0 and ±126 MPa. The average values of the errors for

each locality will be reported in "Depth of Magma Chambers" Section, which reflects the general distribution of pressures for all samples specific localities.

Table 5. Number and percentage of results that have high standard deviation of calculated pressure (σ >126 MPa) are shown. 126 MPa is the uncertainty of the calculation of this method. The high-σ results are considered to be unreliable and not appropriate to be used for data interpretation, and therefore, will be filtered out in process of data filtration. The last column shows the number of sample with standard deviation of calculated pressure that is less than 126 MPa after filtration of high- σ results (but not filtered by any other criteria yet).

Volcanoes	Location/ Eruptive Center	Total # of Samples	Number of Unreliable Pressure (σ >126 MPa)	% of Unreliable Pressures	Number of Pressure with σ ≤126 MPa
Kilauea	Total	592	72	12.2%	520
	*Total Samples without Puna Ridge	552	71	12.9%	481
	Puna Ridge	40	1	2.5%	39
Mauna Kea		579	11	1.9%	568
Mauna Loa		287	17	5.9%	270
Loi'hi		118	42	35.6%	76
Total		1567	142	9.1%	1425

The last two criteria of data filtration are substantially based on observation of the distribution of samples on chemical variation diagrams for each location. The method used for calculating the pressure of partial crystallization is only appropriate for liquid compositions lying on the ol-plag-cpx cotectic, and hence, those glasses that represent liquids in equilibrium with ol, or ol+plag, rather than ol, plag, and cpx, have compositions that are inconsistent with the method of calculation and must be filtered out of the results. Glasses with compositions lying along the ol-plag-cpx liquid line of descent (LLD) will form a well-defined array on variation diagrams, Samples with compositions that plot off this array cannot be confidently considered to be in equilibrium with ol, plag, and cpx, and can also be filtered out of the results. To describe the process involved in these two steps of filtration, variation diagrams of CaO vs MgO, Al_2O_3 vs MgO, and CaO/Al_2O_3 vs MgO are plotted (Figure 9–13). These diagrams were chosen because they involve the chemical components that best describe the compositional differences among the minerals cpx, plag, and ol.

The vast majority of melts crystallize ol during ascent from the mantle, which is called polybaric crystallization (Kelly & Barton, 2008). This type of crystallization produces liquids that move directly away from olivine forming a trend that crosses the ol-plag-cpx cotectics at different pressures on the pseudoternary plane (Figure 5b). In addition, melts that crystallize ol-plag-cpx only can only exist over a certain range of pressures. In other words, below a certain pressure/depth (the upper limit of pressure), no cpx crystals can be formed. Also it follows from Figure 5b that in the region between the highest pressure ol-plag-cpx LLC and the bottom left apex only ol (± plag) but no cpx can crystallize, so that the highest pressure ol-plag-cpx represents the upper limit for pressure of crystallization along the ol-plag-cpx cotectic. In other words, compositions that do not lie on the cotectic can be used to place constraints on the pressures of crystallization, but cannot be used to calculate accurate values of the pressure of crystallization.

The change from liquid compositions that crystallize ol to those that crystallize ol-plag-cpx can be observed on Pressure vs MgO diagrams (Figure 8), but a more effective and reliable method to examine this change is provided by plots of CaO vs MgO, Al_2O_3 vs MgO, and CaO/Al_2O_3 vs MgO variation diagrams together. On these three variation diagrams the liquids that crystallize ol, plag, and cpx can be distinguished from the liquids that crystallize ol, because the trend of increasing CaO and Al_2O_3 and near constant CaO/Al_2O_3 with decreasing MgO indicates the crystallization of ol alone (n.b., ol contains virtually no CaO or Al_2O_3), as shown on Figures 9–13 (a) and (c). Within this trend, as ol (but no cpx or plag) crystallizes from the melts, the amount of MgO will be reduced whereas the amount of CaO and Al_2O_3 increase and the CaO/Al_2O_3 ratio will remain constant. In contrast, when the liquids crystallize ol, plag, and cpx, the contents of MgO, Al_2O_3 and CaO will all decrease. Accordingly, there will be positive correlations between CaO, Al_2O_3, the ratio of CaO/ Al_2O_3 and MgO.

The filtered datasets for the five localities (filtered using the first three criteria) are plotted (Figure 9–13) for purpose of determining the inflection point marking the change from ol to ol-plag-cpx crystallization. There are several reasons for using the dataset filtered using the three criteria rather than the unfiltered dataset to determine the inflection point. First, the non-basaltic samples are filtered out we are interested in the partial crystallization of basalt. Compositional data for samples that yield pressures more negative than -1.26 GPa are removed to allow a more meaningful comparison of conclusions drawn from variation diagrams with those made from plots of P vs MgO. The position of the inflection point defined in terms of the MgO content derived from analysis of the variation diagrams should correspond exactly with the value of the inflection point inferred from P-MgO plots. Inclusion of results for all samples that yield negative pressures on P vs MgO diagram complicates identification of the inflection point on such diagrams (see Figure 8). In contrast, the inflection point is more easily located if results with negative pressures are filtered out (see, for example, Figure 12). For samples belonging to the low-MgO groups (i.e., lying along ol-plag-cpx LLD's), there is no correlation of P and MgO, but the data can be approximately fitted by a set of parallel horizontal lines and the inflection point can be identified more clearly on the diagram. Pressures associated with large uncertainties (1σ) are considered unreliable and are removed for a similar reason. The results for such samples may not reflect the real trends on P vs MgO diagram, especially when the pressures are abnormally high or low and plot away from the trends formed by the reliable results. Furthermore, if the large uncertainty is caused by the errors in measurement of major element compositions (e.g., during analysis with the electron microprobe), the reported compositions of

these samples are questionable and this means that correctly identifying the position of the inflection point on variation diagrams could be adversely affected.

The method used to define the MgO content of the inflection point is to fit polynomial curves to the CaO vs MgO and CaO/Al_2O_3 vs MgO (Figures 9–13 a & c). There is considerable scatter in the variation diagrams for these components, but, rather than indicating weak correlation between MgO and CaO (or MgO and CaO/Al_2O_3), scatter may indicate magma evolution along more than one pressure-dependent liquid line of descent (Herzberg, 2004; Kelly & Barton, 2008). Theoretically, on both CaO vs MgO and CaO/Al_2O_3 vs MgO plots, a series of parallel curves with the same slope could be fitted for the low MgO samples that represent melts in equilibrium with ol-plag-cpx. However, a practical way to estimate the inflection point is to use polynomial regression to fit a curve based on the distribution of samples. In this study, there are several outliers on both diagrams of CaO vs MgO and Al_2O_3 vs MgO of Mauna Loa (Figure 13). These outliers have compositions that plot off the array defined by the majority of the glasses, and were removed before polynomial fitting. The fitted curves describe not just position of the ol-plag-cpx cotectic on the plots, but also the LLD for olivine crystallization. Therefore, the inflection point on the curve can be considered as the starting point (in terms of MgO content) for liquids that crystallize ol-plag-cpx. The MgO content of the inflection points is determined by differentiating the polynomial equations and by averaging the two values obtained for the inflection points in shown on the CaO vs MgO and CaO/Al_2O_3 vs MgO plots, respectively. This average value is also plotted on diagrams Al_2O_3 vs MgO and on diagrams of Pressure vs MgO. Variation diagrams of Al_2O_3 vs MgO (Figures 9–13 b) are plotted to observe any unusual changes of Al_2O_3 content that might affect the value of CaO/Al_2O_3 and hence to ensure the reliability of the lines fitted on CaO/Al_2O_3 vs MgO diagrams (Figures 9–13 c). The calculated values of the inflection points are also plotted on Pressure vs MgO diagrams (Figures 9–13 d) to verify this value correctly divides the two lines identified on these diagrams.

In this study, the change from liquids that crystallize ol-plag-cpx and those crystallize ol is ~7 wt. % MgO for samples from all localities on the Island of Hawaii. This calculated value of inflection point also separates the two groups identified on P vs MgO diagrams. This is particularly the case for the filtered datasets for Kilauea, Mauna Kea, and Mauna Loa. Puna Ridge only has samples belonging to the MgO group, whereas many of the samples that were originally in the high MgO group for Lo'ihi have been filtered out of this dataset. The negative correlation between P and MgO is preserved for the low MgO group in the filtered dataset for Lo'ihi. Use of other polynomial equations (e.g., 4 degree rather than 3 degree polynomial curving fitting) to estimate the position of inflection point might generate slightly different value MgO wt. % for filtration criterion.

Filtration based removal of samples that plot off the ol-plag-cpx liquid line of descent (LLD) defined by the vast majority of samples was done using the CaO vs MgO, Al_2O_3 vs MgO, and CaO/Al_2O_3 vs MgO variation diagrams (Figure 9–13 a–c) and the five steps of data filtration are shown on Figure 14. For low MgO samples, only Lo'ihi and Mauna Loa have distinct compositional outliers, and those samples have been removed by other steps of data filtration. The number of samples filtered out using the different criteria is summarized in Table 6.

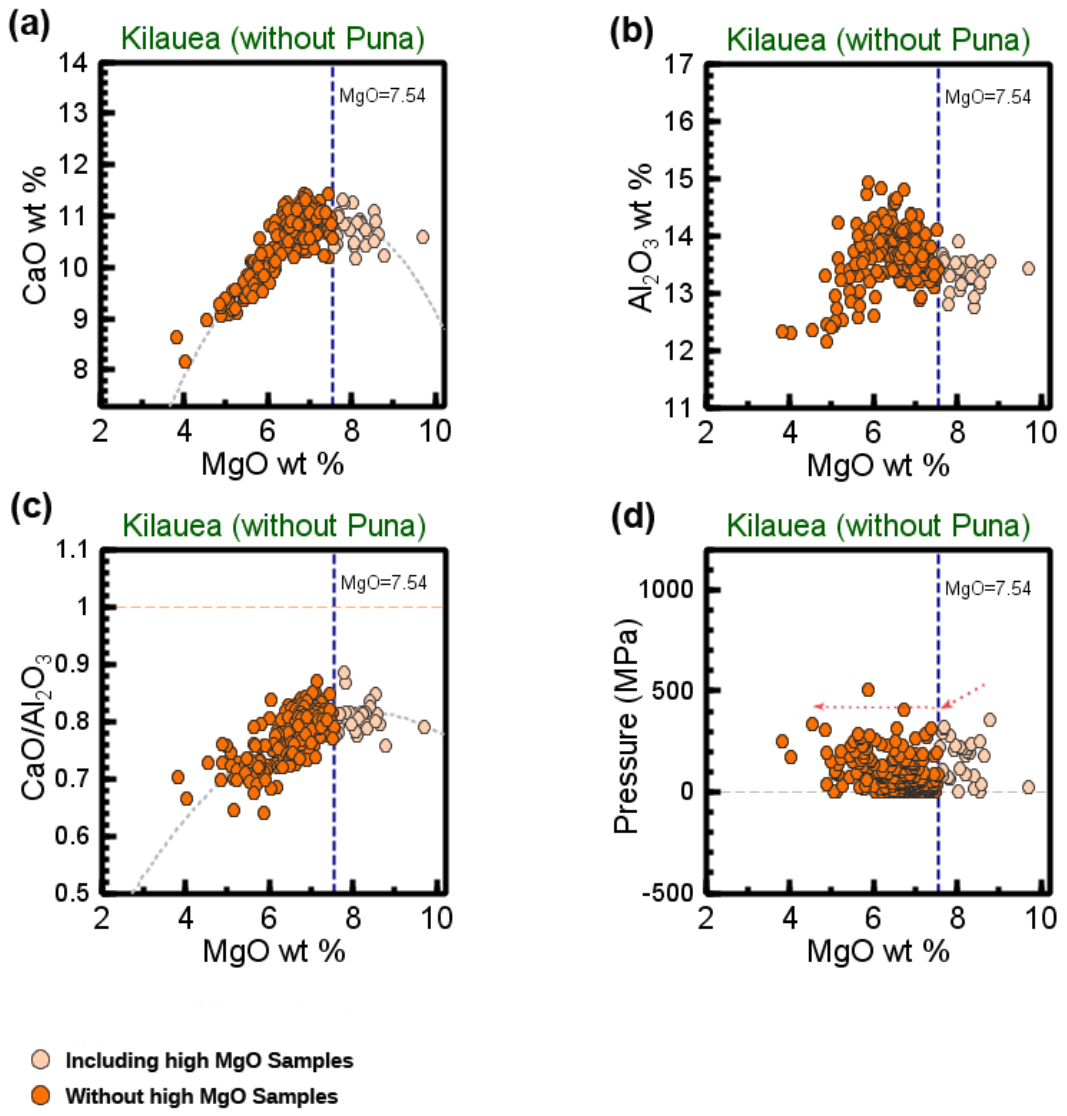

Figure 9. Variation diagrams of CaO vs MgO, Al_2O_3 vs MgO, CaO/Al_2O_3 vs MgO and pressure vs MgO for samples from Kilauea (without Puna Ridge). Same scale of MgO wt. % axis is plotted on these four diagrams for comparing the changes of trend from each other. The total samples on each diagram has been filtered and corrected by three other criteria: non-basalt, negative pressure, high calculated standard deviation. And samples of high MgO content that crystallize *ol-plag* (light orange) and those of low MgO content that crystallize *ol-plag-cpx* (orange) are included in the total samples. The blue dash line represents the criteria of MgO content to distinguish the high MgO samples from low MgO samples, which is defined by the inflection point on the fitting curves on **(a)** and **(c)**.

In **(a)** and **(c)**, increasing CaO wt. % and CaO/Al_2O_3 with decreasing MgO wt. % of high MgO samples can be distinguished from decreasing CaO wt. % and CaO/Al_2O_3 with decreasing MgO wt. % of low MgO samples. The grey curves fitted to the data are plotted to identify these two observations. In **(c)**, the ratio of CaO/Al_2O_3=1 is marked by light orange dash line. Composition of samples with CaO/Al_2O_3>1 could result from assimilation of *cpx*. In **(d)**, the red arrows represent the two trends of pressure versus MgO content. For samples with high MgO, pressure decreases with decreasing MgO content, whereas for samples with low MgO, there is no correction between pressure and MgO content (marked by arrow with horizontal line).

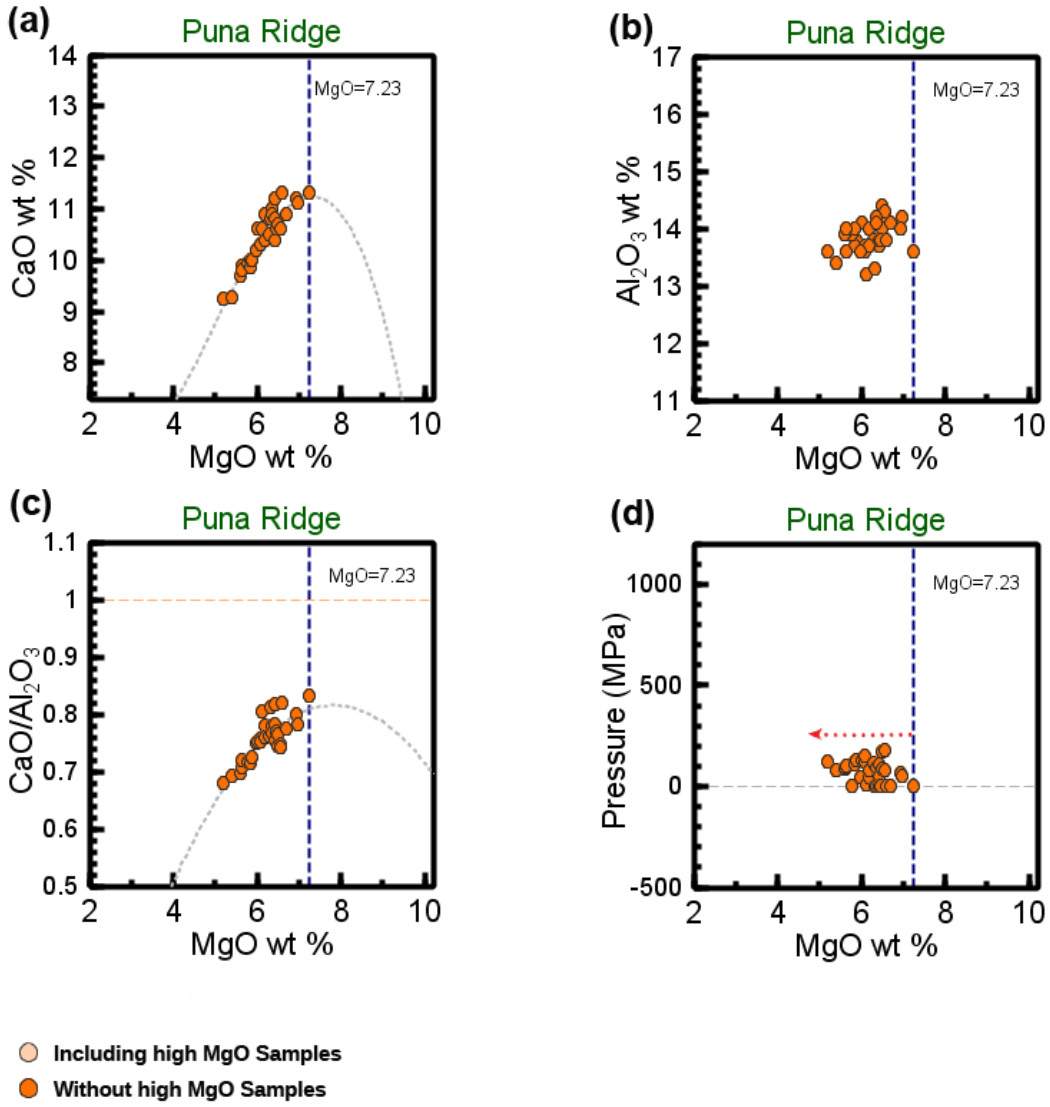

Figure 10. Variation diagrams of CaO vs MgO, Al_2O_3 vs MgO, CaO/Al_2O_3 vs MgO and pressure vs MgO for samples from Puna Ridge. Same scale of MgO wt. % axis is plotted on these four diagrams for comparing the changes of trend from each other. The total samples on each diagram has been filtered and corrected by three other criteria: non-basalt, negative pressure, high calculated standard deviation. Samples of low MgO content that crystallize *ol-plag-cpx* are marked in orange. However, no samples of high MgO content that crystallize *ol-plag* are shown. The blue dash line represents the criteria of MgO content to distinguish the high MgO samples from low MgO samples, which is defined by the inflection point on the fitting curves on **(a)** and **(c)**.

In **(a)** and **(c)**, the grey fitting curves are plotted to distinguish the trend of increasing CaO wt. % and CaO/Al_2O_3 with decreasing MgO wt. % of high MgO samples from the trend of decreasing CaO wt. % and CaO/Al_2O_3 with decreasing MgO wt. % of low MgO samples. In **(c)**, the ratio of CaO/Al_2O_3=1 is marked by light orange dash line. Composition of samples with CaO/Al_2O_3>1 could result from assimilation of *cpx*. In **(d)**, the red arrow with horizontal line indicates that there is no correction between pressure and MgO content for low MgO samples.

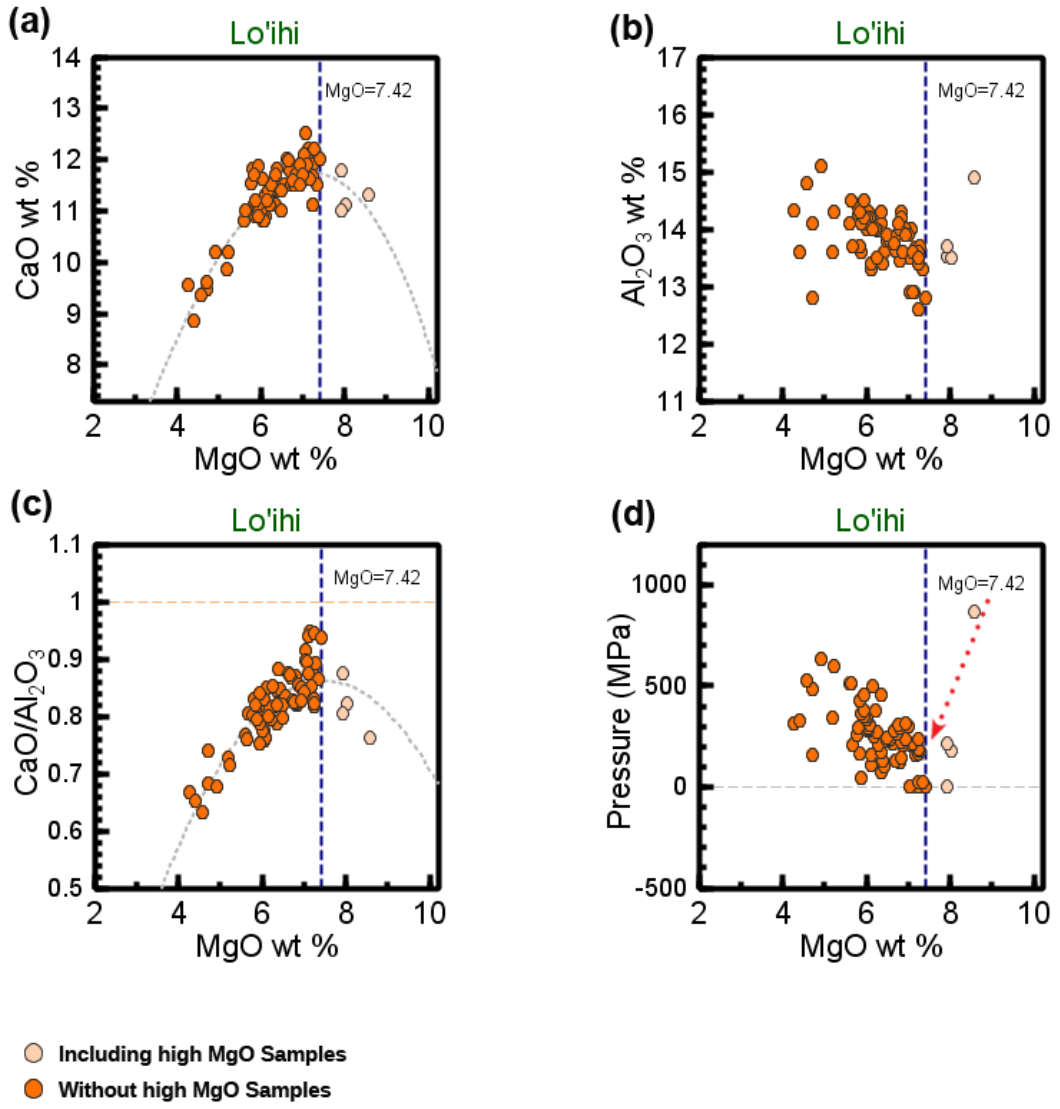

Figure 11. Variation diagrams of CaO vs MgO, Al_2O_3 vs MgO, CaO/Al_2O_3 vs MgO and pressure vs MgO for samples from Loi'hi. Same scale of MgO wt. % axis is plotted on these four diagrams for comparing the changes of trend from each other. The total samples on each diagram has been filtered and corrected by three other criteria: non-basalt, negative pressure, high calculated standard deviation. And samples of high MgO content that crystallize *ol-plag* (light orange) and those of low MgO content that crystallize *ol-plag-cpx* (orange) are included in the total samples. The blue dash line represents the criteria of MgO content to distinguish the high MgO samples from low MgO samples, which is defined by the inflection point on the fitting curves on **(a)** and **(c)**.

In **(a)** and **(c)**, the increasing CaO wt. % and CaO/Al_2O_3 with decreasing MgO wt. % of high MgO samples can be distinguished from the samples showing decreasing CaO wt. % and CaO/Al_2O_3 with decreasing MgO wt. % of low MgO samples. The grey fitted curves are plotted to identify these two trends. In **(c)**, the ratio of CaO/Al_2O_3=1 is marked by light orange dash line. Composition of samples with CaO/Al_2O_3>1 could result from assimilation of *cpx*. In **(d)**, the one red arrows represent the trend that pressure decreases with decreasing MgO content for high MgO samples. However, Loi'hi shows an unusual trend for low MgO samples, increasing pressure with decreasing MgO content.

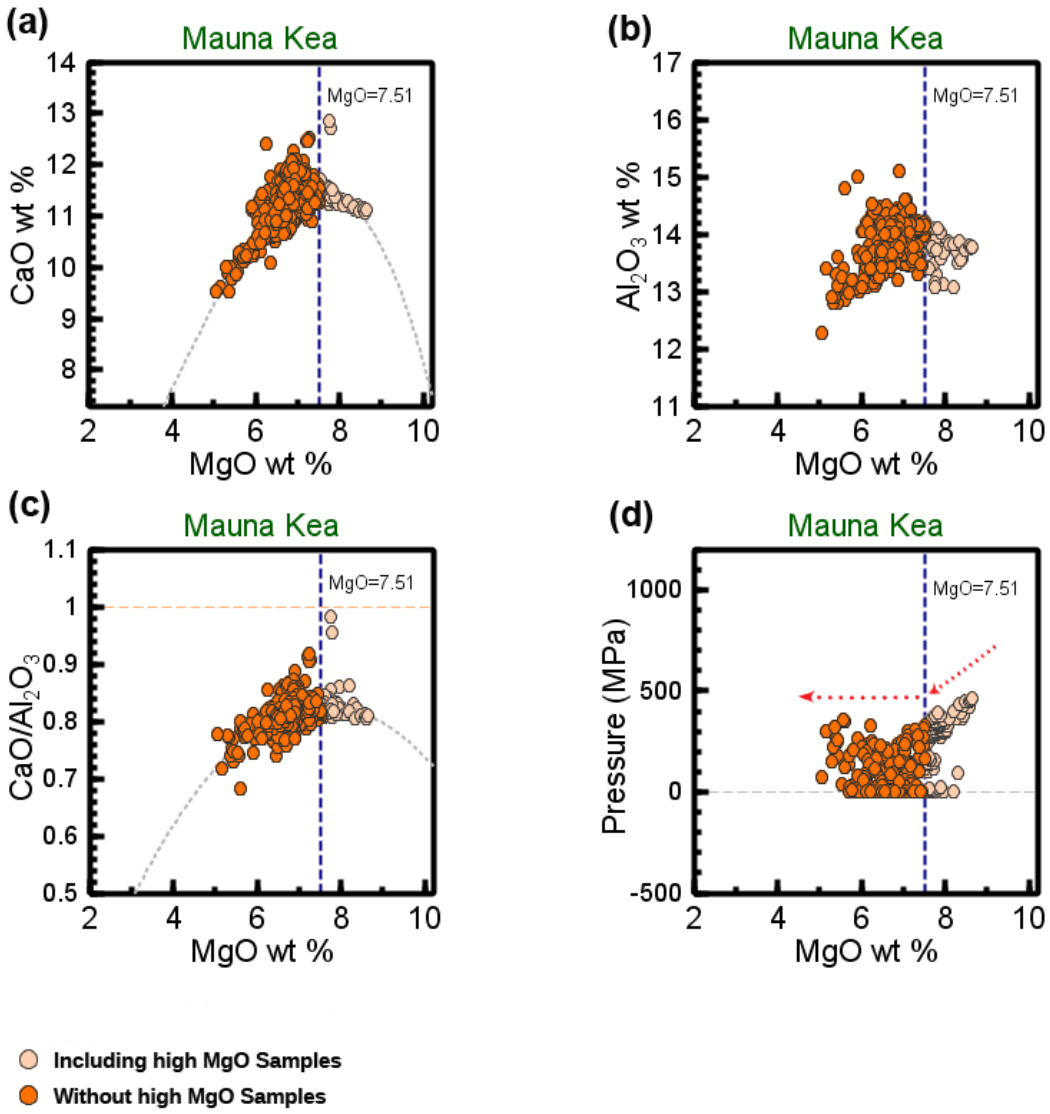

Figure 12. Variation diagrams of CaO vs MgO, Al_2O_3 vs MgO, CaO/Al_2O_3 vs MgO and pressure vs MgO for samples from Mauna Kea. Same scale of MgO wt. % axis is plotted on these four diagrams for comparing the changes of trend from each other. The total samples on each diagram has been filtered and corrected by three other criteria: non-basalt, negative pressure, high calculated standard deviation. And samples of high MgO content that crystallize *ol-plag* (light orange) and those of low MgO content that crystallize *ol-plag-cpx* (orange) are included in the total samples. The blue dash line represents the criteria of MgO content to distinguish the high MgO samples from low MgO samples, which is defined by the inflection point on the fitting curves on **(a)** and **(c)**.

In **(a)** and **(c)**, the increasing CaO wt. % and CaO/Al_2O_3 with decreasing MgO wt. % of high MgO samples can be distinguished from samples showing decreasing CaO wt. % and CaO/Al_2O_3 with decreasing MgO wt. % of low MgO samples. The grey fitted curves are plotted to identify these two groups of samples. In **(c)**, the ratio of CaO/Al_2O_3=1 is marked by light orange dash line. Composition of samples with CaO/Al_2O_3>1 could result from assimilation of *cpx*. In **(d)**, the red arrows represent the two trends of pressure versus MgO content. For samples with high MgO, pressure decreases with decreasing MgO content, whereas for samples with low MgO, there is no correction between pressure and MgO content (marked by arrow with horizontal line).

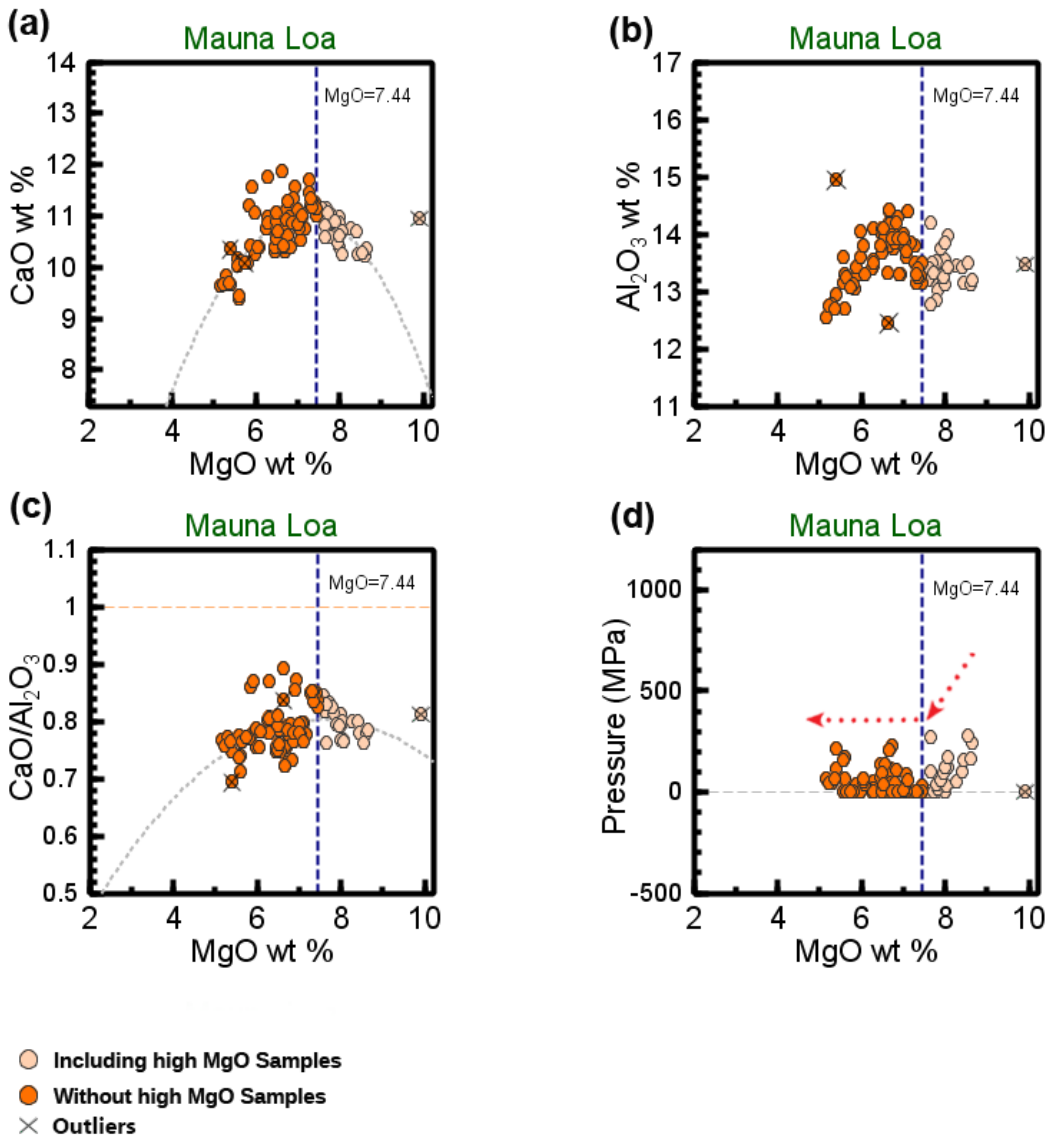

Figure 13. Variation diagrams of CaO vs MgO, Al_2O_3 vs MgO, CaO/Al_2O_3 vs MgO and pressure vs MgO for samples from Mauna Loa. Same scale of MgO wt. % axis is plotted on these four diagrams for comparing the changes of trend from each other. The total samples on each diagram has been filtered and corrected by three other criteria: non-basalt, negative pressure, high calculated standard deviation. And samples of high MgO content that crystallize *ol-plag* (light orange) and those of low MgO content that crystallize *ol-plag-cpx* (orange) are included in the total samples. The blue dash line represents the criteria of MgO content to distinguish the high MgO samples from low MgO samples, which is defined by the inflection point on the fitting curves on **(a)** and **(c)**.

In **(a)** and **(c)**, the trend of increasing CaO wt. % and CaO/Al_2O_3 with decreasing MgO wt. % of high MgO samples can be distinguished from the trend of decreasing CaO wt. % and CaO/Al_2O_3 with decreasing MgO wt. % of low MgO samples. The grey fitting curves are plotted to identify these two trends. The outliers marked by "x" are removed before curve fiting. In **(c)**, the ratio of CaO/Al_2O_3=1 is marked by light orange dash line. Composition of samples with CaO/Al_2O_3>1 could result from assimilation of *cpx*. In **(d)**, the red arrows represent the two trends of pressure versus MgO content. For samples with high MgO, pressure decreases with decreasing MgO content, whereas for samples with low MgO, there is no correction between pressure and MgO content (marked by arrow with horizontal line).

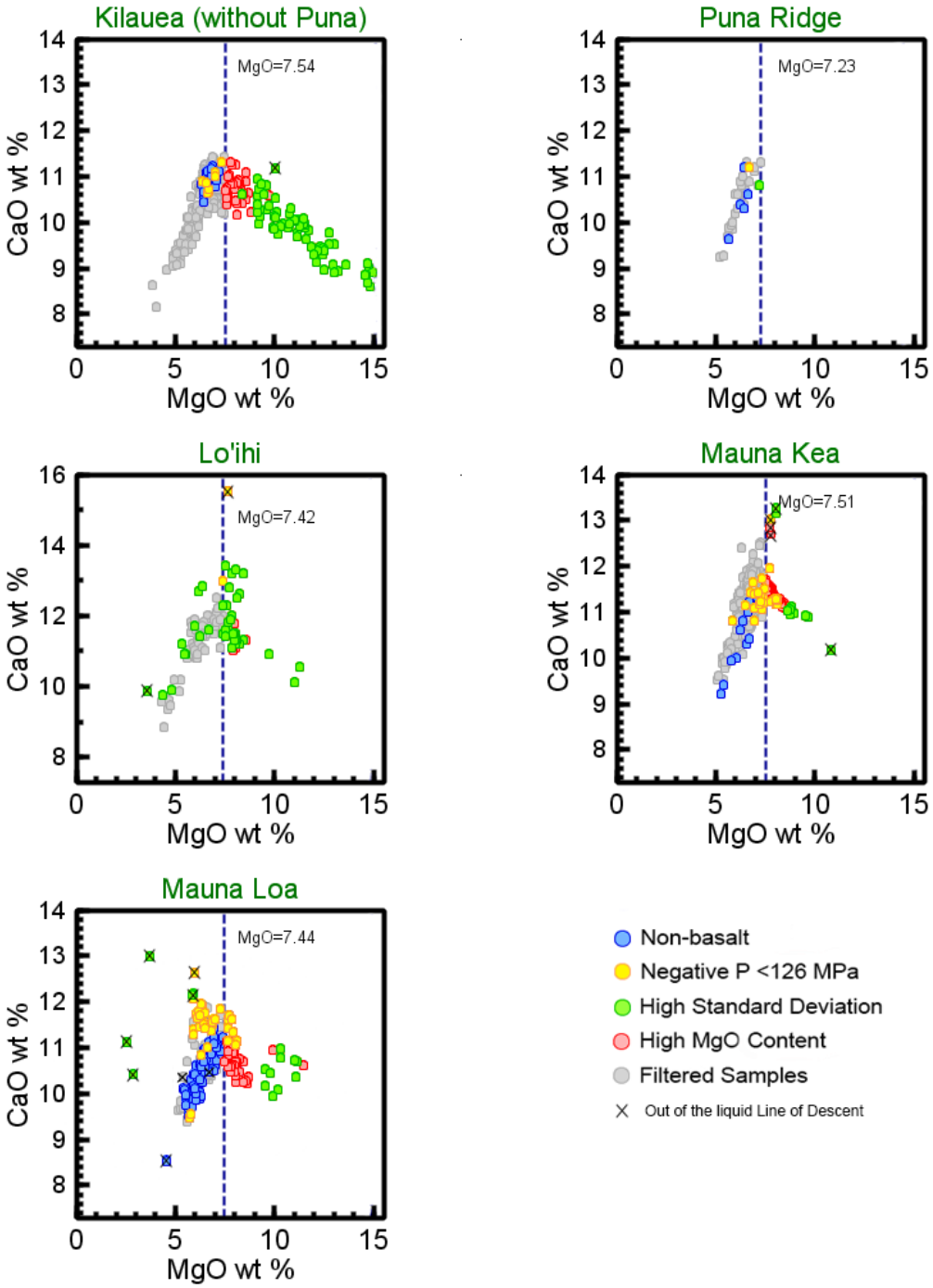

Figure 14. Variation diagrams of CaO vs MgO wt. % for five locations to summarize the process of data filtration in five steps. Samples in color blue, yellow, green, and red and marked by "x" will be filtered out. Samples that have filtered by 5 steps (grey) will be used as final results for pressure (and depth) interpretation. In the Mauna Loa plot, the two samples marked outliers lying on the trend of CaO vs MgO are selected by correlation of Al_2O_3 vs MgO. The number of samples in each category can be found in Table 6.

Table 6. Number of results that are not appropriate to be used for data interpretation and will be filtered out in process of data filtration. The inappropriate results include those that are non-basaltic, of unreliable unrealistic pressure (calculated σ >126 MPa), of unrealistic pressure (negative pressures that are less than -126 MPa), not with crystallization of ol-plag-cpx (with high MgO content, wt. % >7%), and not lying on ol-plag-cpx Liquid Line of Descent (listed in column 4 to column 8). The number total calculated results (same as input data) are shown in column 3, while the number of final results after data filtration of 5 different criteria is shown in the last column. *In column 6, the number of "Unrealistic Pressures (< -126MPa)" that will be filtered out is equal to the number of total results of negative pressure minus the number of those with pressure < -126 MPa in Table 4.

Volcanoes	Location/ Eruptive Center	Total # of Samples	Non-basaltic	Unreliable Pressure	Unrealistic Pressure (< -126MPa)	Not with Crystallization of ol-plag-cpx	Not on ol-plag-cpx Liquid Line of Descent	Final Results for Interpretation
Kilauea	Total	592	42	72	9	105	0	438
	*Total Number without Puna	552	37	71	8	105	0	405
	Puna Ridge	40	5	1	1	0	0	33
Mauna Kea		579	17	11	27	99	0	446
Mauna Loa		287	158	17	42	54	6	72
Loi'hi		118	3	42	5	34	2	69
Total		1567	220	142	83	292	8	1027

Effect of Mg-Fe Exchange in Melt Inclusions

During the process of differentiation, MgO content decreases as the basalts partially crystallize and differentiation of tholeiitic magma results in an iron-enrichment trend that is clearly seen on FeO* vs MgO variation diagrams. A strong negative correlation of MgO and FeO wt. % for samples with MgO <~7% is seen for the Kilauea (without Pu'u'O'o and Puna Ridge), Pu'u'O'u, Puna Ridge, Mauna Kea and Loi'hi glasses, although the correlation is less strong for the latter (Figure 15). There is considerable scatter for the data from Mauna Loa on plots of MgO versus FeO content and it is hard to identify the iron-enrichment trend. Samples that do not lie on an iron-enrichment line are probably not appropriate for use to estimate pressure because these samples may not represent true, erupted liquid compositions formed by differentiation of tholeiitic basalts.

A significant proportion (~30%, 85 out of 287) of glasses in the database for Mauna Loa were analyzed in olivine-hosted melt inclusions. A possible explanation for the scatter on plots of MgO versus FeO (and hence for weak correlations between MgO and FeO) is the exchange of Mg^{2+} and Fe^{2+} between the host olivine and included glass during cooling. Melt inclusions in all minerals are associated with hydrogen diffusion into and out of the inclusions, and the re-equilibration of melt inclusions with host phenocrysts results in changes of the liquid composition (Danyushevsky et al, 2002). As a result of exchange of ions between the inclusion and host, most melt inclusions in forstritic olivine phenocrysts trend to have higher MgO and Low FeO contents than those of the melts before trapping. This effect is commonly observed for subduction-related and within-plate lavas (Danyushevsky et al, 2002), and appears to be true for many Mauna Loa samples of glass inclusions in the study of Davis et al. (2003). The controls on Fe-Mg exchange include pressure, temperature, and the olivine and liquid compositions (Laubier et al. 2007). Post-entrapment modification of melt inclusions is consistent with the characteristics of the Mauna Loa dataset used in this study. As shown in the FeO* vs MgO diagrams, data for samples of matrix glasses display a relatively tight, strong iron-enrichment trend (Figure 16 (b) and (d)), whereas there is a large amount of scatter on those diagrams with data for matrix glasses and glass inclusions plotted (Figure 16 (a) and (c)).

It is necessary to remove samples with anomalous MgO and FeO contents from the dataset because such samples have compositions that do not lie on an ol-plag-cpx cotectic and will yield unreliable estimates of the pressure of partial crystallization. This problem was found also for a large number of glass inclusion analyses in samples from Iceland by Barton and Kelley (2008). Note also that and the composition of other major elements would be affected by re-equilibration of MgO and FeO between the trapped glass and olivine host. According to Davis et al (2003) many analyses of glass inclusions from Mauna Loa have higher CaO, lower K_2O and lower Al_2O_3 than the matrix glass.

Samples of inclusion glasses with anomalous compositions can be filtered out of the database based on examination of variation diagrams (see also Barton and Kelley, 2008) and by using the other criteria for data filtration described in a previous section. The samples filtered out of the dataset (including some samples of matrix glasses) are shown in Figure 18. The remaining samples (Figure 17 & 18) display a strong correlation between MgO and FeO similar to that shown by samples from the other volcanic center. In conclusion, therefore, the effects of Fe-Mg ion exchange haves been removed from the filtered dataset for Mauna Loa in this study.

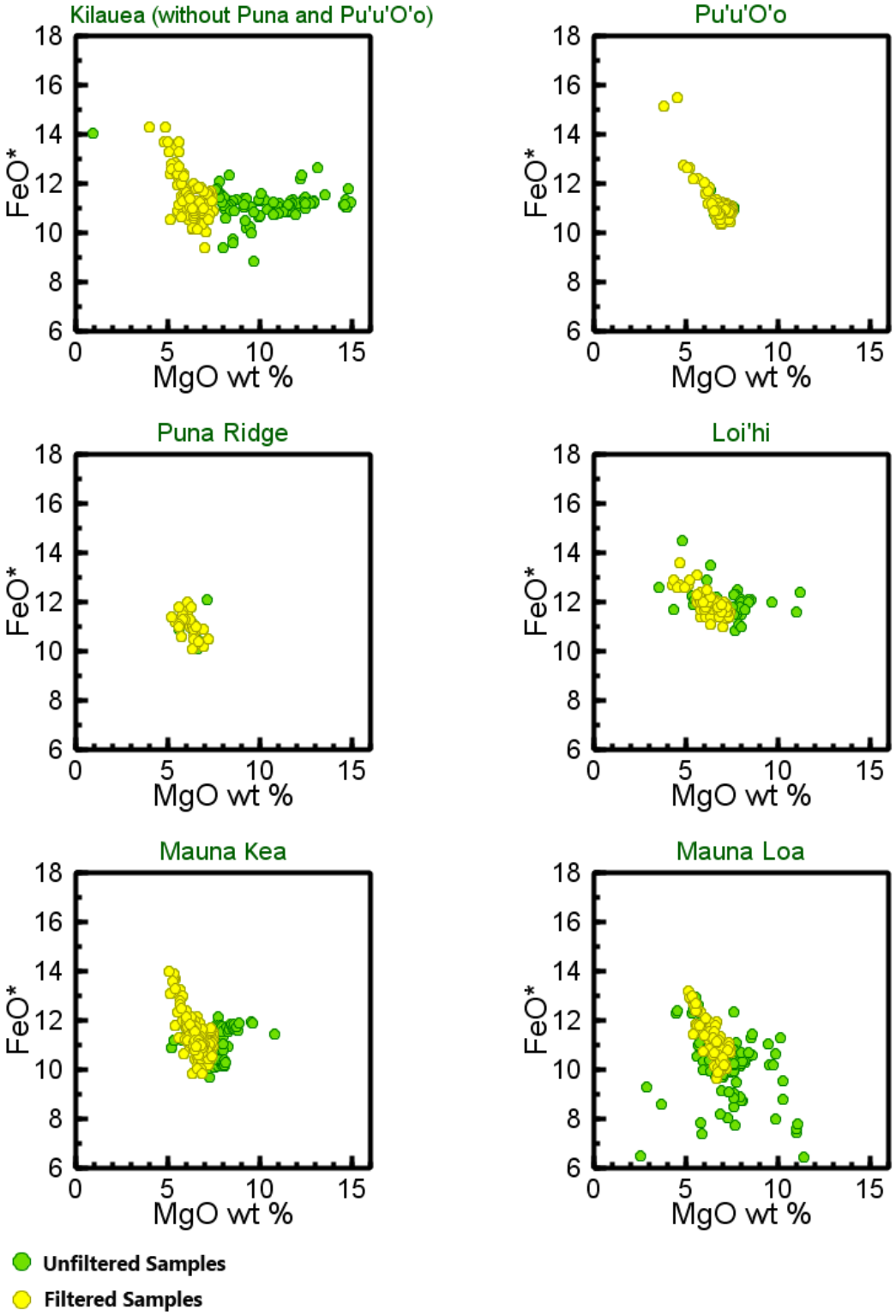

Figure 15. FeO* (wt. % total Fe as FeO) vs MgO wt. % of samples from 6 locations. Samples from Puna Ridge and Pu'u'O'o Volcanic Cone are separated from other samples from Kilauea. Satters of unfiltered samples from Mauna Loa indicates Mg-Fe exchange between inclusion and olivine. The filtered samples on each plot show a negative linear relationship between MgO and FeO*, indicating iron enrichment during differentiation.

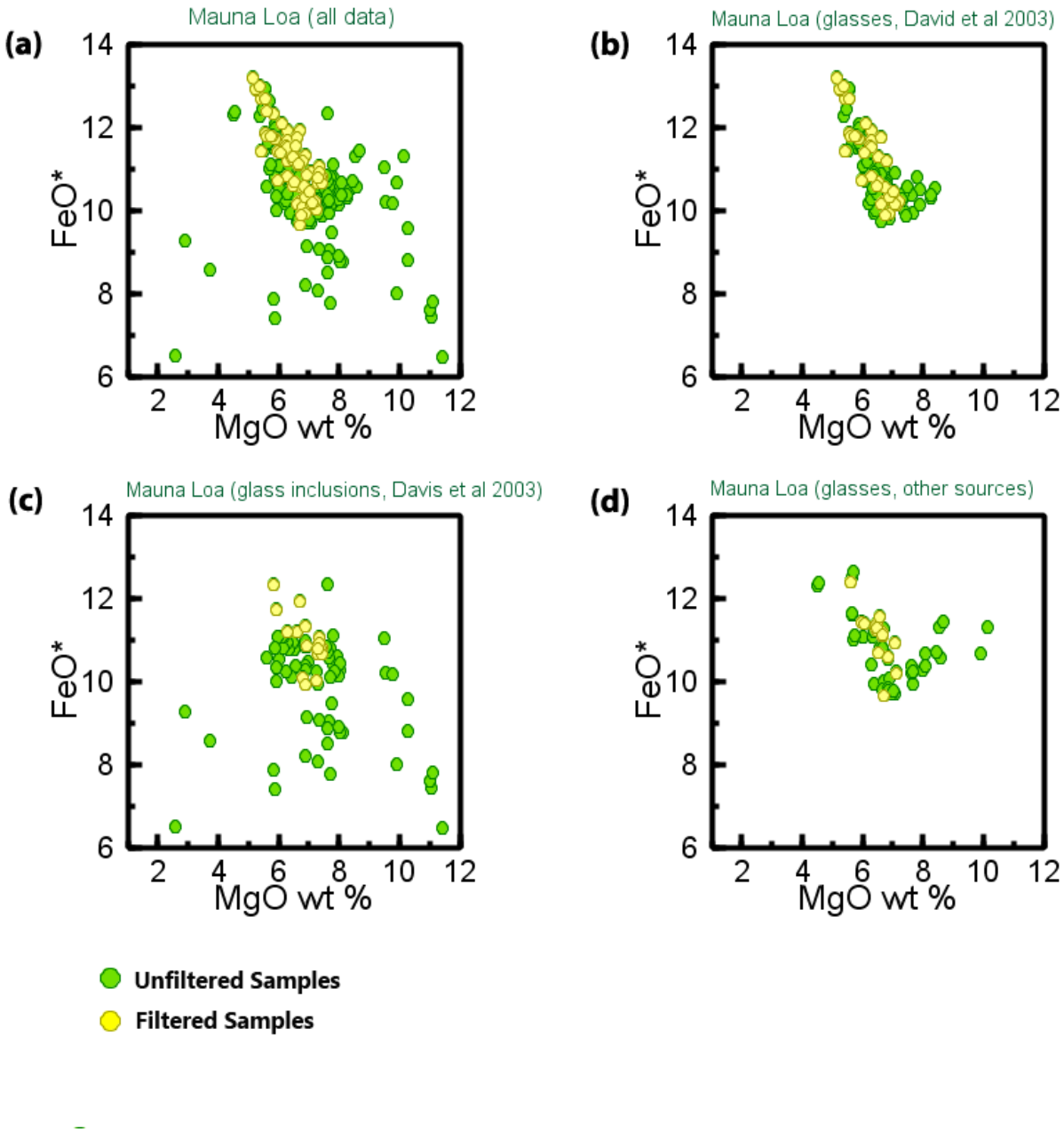

Figure 16. FeO* (wt. % total Fe as FeO) vs MgO wt. % of samples from Mauna Loa. The total samples from Mauna Loa are shown in **(a)** and samples are sorted by sources on the other plots. In **(b)** and **(d)**, both unfiltered and filtered glass sample show negative relationship between MgO and FeO*. However, a plot of scatter of unfiltered samples are shown in **(c)**, the dataset of olivine-hosted glass inclusions, indicating Mg-Fe exchange between inclusion and olivine.

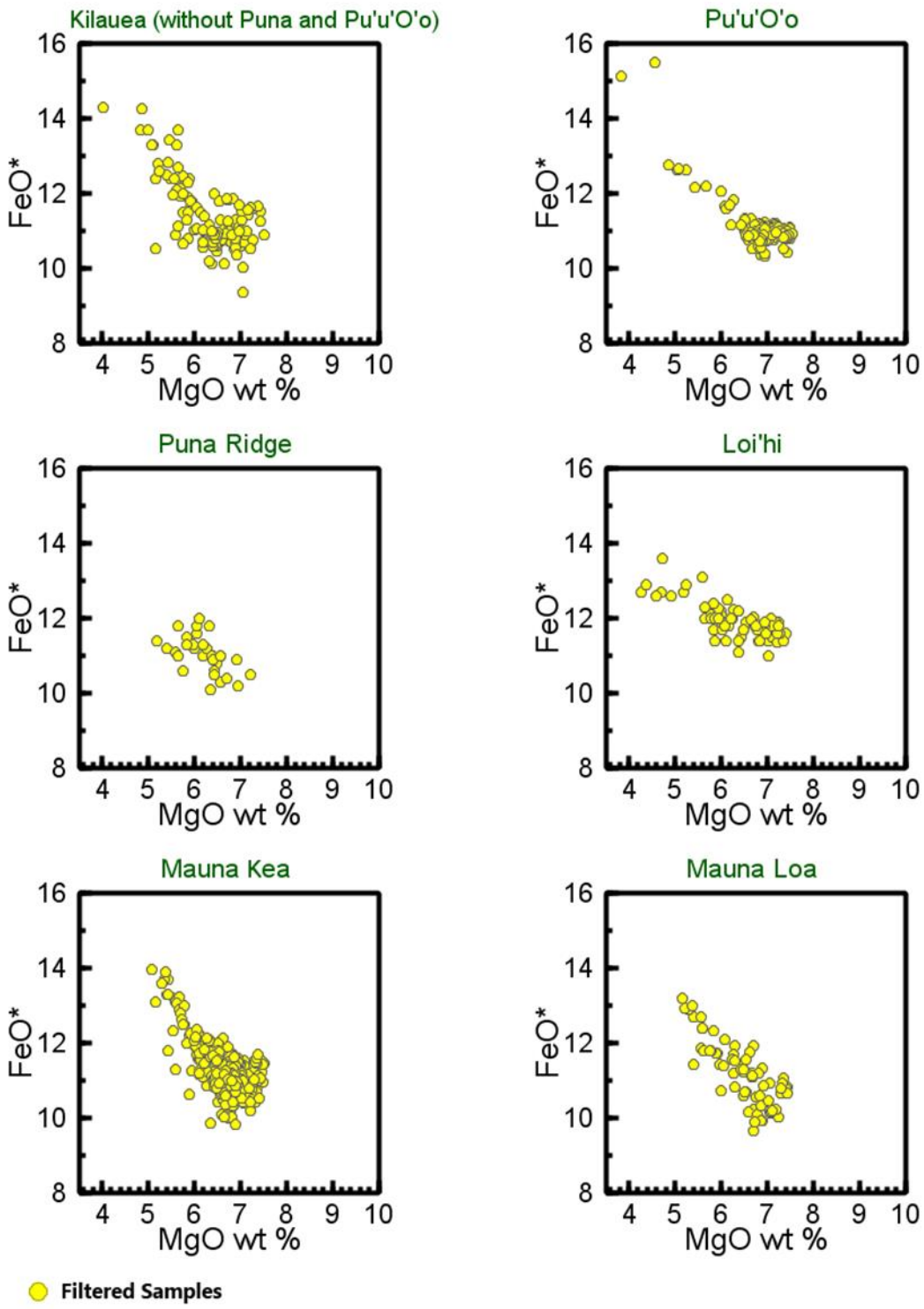

Figure 17. FeO* (wt. % total Fe as FeO) vs MgO wt. % of filtered samples from 6 locations. Samples from Puna Ridge and Pu'u'O'o Volcanic Cone are separated from other samples from Kilauea. Negative relationship between MgO and FeO* on each plot indicates the iron enrichment during differentiation.

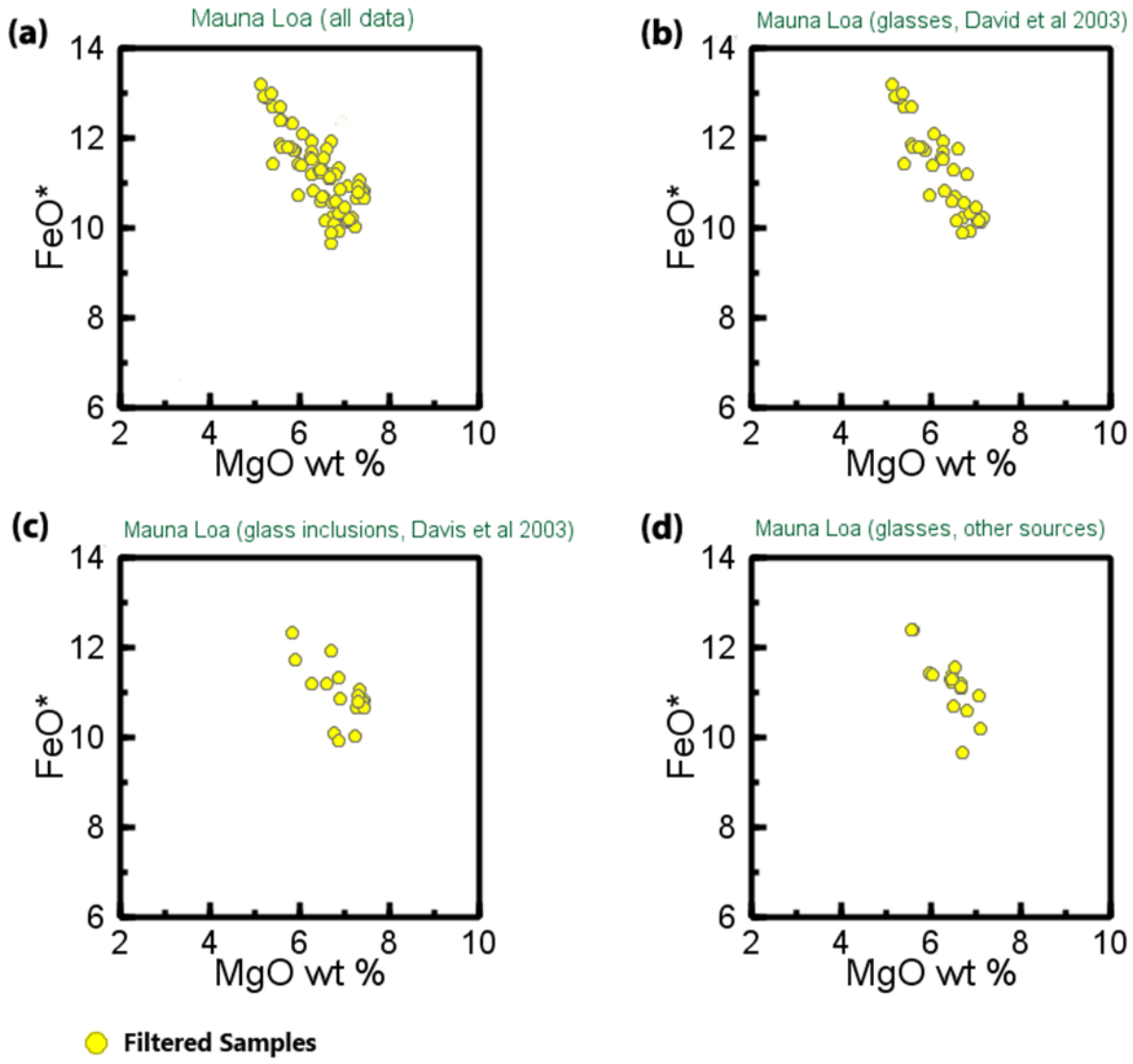

Figure 18. FeO* (wt. % total Fe as FeO) vs MgO wt. % of filtered samples from Mauna Loa. The total samples from Mauna Loa are shown in **(a)** and samples are sorted by sources on the other plots. Samples in each plot show negative relationship between MgO and FeO*.

Interpretation of Calculated Pressures

The chemical compositions of the glasses provide information about magma evolution. The relationships on variation diagrams such as CaO vs MgO and CaO/Al_2O_3 vs MgO can together be used to distinguish between those liquid compositions in equilibrium with ol-plag-cpx and those in equilibrium with ol. The former represent liquids crystallizing along ol-plag-cpx cotectics. Those liquid compositions crystallizing only ol lack the signature of cpx crystallization and might have formed at a pressure beyond the upper limit of cpx and plag saturation. The relationship between pressure and MgO is shown for the data sets filtered using the first three quantitative criteria in Figures 9–13 (d). The dataset for Puna Ridge does not contain MgO-rich (>~7%) samples. The range of pressures for MgO-rich samples from Kilauea (without Puna Ridge), is about the same as that for samples that crystallized in equilibrium of ol-plag-cpx, and therefore filtering out results for these samples does not affect conclusions about the pressure of partial crystallization of Kilauea magmas. The range of pressures for MgO-rich samples from Mauna Kea and Mauna Loa is slightly larger than that for samples crystallizing in equilibrium with ol-plag-cpx. In the case of Lo'ihi, most of the MgO-rich samples have been filtered out of the results, but the pressure calculated for one of the remaining samples is higher than that for samples that crystallized in equilibrium with ol-plag-cpx. These MgO-rich samples do not carry a signature of cpx and plag crystallization, so that it cannot be concluded from these results that some represent samples that actually crystallized at higher pressure than the samples that crystallized in equilibrium with ol-plag-cpx.

The results clearly suggest that partial crystallization of samples with compositions lying on an ol-plag-cpx cotectic occurred over a wide range of pressures, suggesting polybaric evolution of magmas beneath all of the volcanoes included in this study. However, the interpretation of the results is not straightforward, because magma evolution can be complex and involve processes other than crystallization. Two such processes are magma mixing and assimilation, and the effects of these processes on calculated pressures of partial crystallization have been discussed in details by Kelly and Barton (2008). The mixing between primitive melt and evolved melt lying along the same cotectic will produce a hybrid magma of intermediate composition but will have no effect on the calculated pressures of partial crystallization. The mixing between a melt lying along a high-pressure cotectic and a melt lying along a low-pressure cotectic will also produce a hybrid magma of intermediate composition, and the pressures of partial crystallization of this hybrid will lie between the values calculated for the end-members involved in mixing. Therefore, mixing will produce a smaller range of pressures than that shown by the pre-mixing end-member compositions rather than a wide range of pressure. The effects of crystallization of ol±plag during ascent accompanied by dissolution and assimilation of cpx from gabbroic crust will generate contaminated magmas with higher CaO contents and higher CaO/Al_2O_3 ratios than mamas produced by crystallization alone. Calculated pressures for such magmas will be lower than the pressure of partial crystallization of associated uncontaminated magmas (Kelley and Barton, 2008). The samples in the filtered database used in this study all have $CaO/Al_2O_3<1$ and no samples have anomalously high CaO contents or anomalously high CaO/Al_2O_3 (Figures 9–13). There is evidence from mid-ocean ridge basalts that crystallization of ol±cpx during ascent of some magmas is accompanied by dissolution and assimilation of plag from gabbroic crust (Zerda, 2016). This will generate contaminated magmas with higher content of Al_2O_3 and lower CaO/Al_2O_3 ratios than mamas produced by crystallization alone. Calculated pressures for such magmas will be higher than the pressure of partial crystallization of associated uncontaminated

magmas (Zerda, 2016). None of the sample in the filtered database has anomalously high Al_2O_3 contents or anomalously low CaO/Al_2O_3 ratios.

This discussion does not preclude the possibility that some of the magmas erupted from Hawaiian volcanoes are the products of mixing, or have interacted with crustal material. Indeed, mixing and assimilation are likely to accompany crystallization in dynamic volcanic plumbing systems. However, it is concluded that there is no evidence that the wide range of pressures calculated for glasses in the study is the results of the operation of mixing and/or assimilation. It follows that the wide range of pressures reflects partial crystallization during polybaric evolution of the magmas erupted from the volcanoes on Hawaii.

Depths of Magma Chambers

The pressures and corresponding depths of partial crystallization are plotted versus MgO (wt. %) for the five locations (Figure 19-20). The same scales are used for pressure, depth and wt. % MgO on all figures to facilitate comparison of the results for different locations. Histograms were calculated for the depths obtained at each locality (Figure 21). The class width is 1 km for each location. The expected frequencies of the data are also shown on the histograms, which represent an estimate of the distribution of the populations assuming that the populations are normally distributed. The estimate (expected frequency) is probably not applicable for Lo'ihi as the depths for this location display a distinctly bimodal distribution. The average, maximum, minimum, and range of pressures and depths for the five locations are listed in Table 7 and Table 8. The reported range is for the majority (68.2%) of the assuming a normal distribution and is calculated by taking ± 1 standard deviation of the average pressure or depth for each location. The range calculated for Lo'ihi is of lower significance than for the other localities because the distribution of results for Lo'ihi shows at least two classes of high frequencies of pressure (and depth). The results for Lo'ihi samples deviate from a normal distribution. The upper limit of depth for all locations shown in is 0 km (calculated by filtered data with the correction of negative results) (Figure 19).

The upper limit of uncertainty inherent in the method of calculation is ±126 MPa, but the uncertainty associated with average pressures calculated for each location is much lower. The uncertainty calculated for average pressures is ±28–34 MPa for samples from shield volcanoes, and is ±63 MPa for samples from Lo'ihi. Error bars showing the average value of pressure ± this uncertainty for each location are plotted on Figure 19. An examination of the uncertainty for pressures calculated for individual samples that are higher than those calculated for other samples from the same locality is useful to determine whether the higher pressures are likely to be significant. One example to illustrate use of uncertainties to assess the significance of high pressures calculated for individual samples is shown in Figure 20. One sample for Kilauea yield an anomalously high pressure (compared with other samples) of ~410 MPa (depth ~14 km). The uncertainty associated with this calculated pressure is small, and the result for this sample does not overlap with the results for other samples (error bars shown on Figure 20) that cluster around 290 MPa (~10 km). This suggests that the result obtained for this sample is worthy of attention and indicates actual crystallization at a higher pressure (410 MPa). In addition to the error bars showing on plots (precision), the accuracy of calculation is ±126 MPa (discussed in the Methods section), which represent the highest possible difference between the apparent pressure and the actual pressure, taken from the comparison of calculated pressure and experimental pressure of

glasses studied by Kelly & Barton (2008). However, the actual value of this error for Hawaiian glasses in this study could be lower than ±126 MPa.

The depth of partial crystallization of each sample is calculated from the pressure using the equation in "Converting Pressure to Depth", Methods section. The average density of oceanic crust is used in this calculation. The crustal density is taken as a constant (2900 kg/m^3), that is, an average crustal density is used, although in actuality crustal density generally increases with depth (Becerril et al., 2013). This value can be modified to obtain better estimates of depth if more accurate estimates of the density for specific areas of Hawaiian Islands and various crustal layers are available. If the density is 2900 kg/m^3, 100 MPa is equivalent to 3.52 km, and hence the upper limit of uncertainty in pressure (126 MPa) equals 4.43 km uncertainty in depth. Accordingly, the uncertainty associated with depths associated with the average pressure of crystallization is ~1.0–1.2 km for samples from shield volcanoes, and 2.2 km for samples from Lo'ihi. The average depth of crystallization of lavas from the subaerial portion of Kilauea is 1.77 km (50.8 MPa). The depth-range for crystallization for the majority (~68.2%) of samples is 0–4.55 km (estimated from 1 standard deviation about the average depths calculated for Kilauea. The maximum depth is 17.70 km (503.1 MPa) (Table 7-8). In the plot of pressure/depth vs MgO, a large number of results fall in the range from 0 to 5 km (Figure 19). A smaller number of results fall in the range 5–12 km, and two samples plot at 14.4 km and 17.7 km. In the histogram, the frequency shows a progressive decline from 0 to ~11 km, with the two samples forming outliers at greater depths (Figure 21).

Samples from the eastern submarine extension of Kilauea, the Puna Ridge, crystallized at an average depth of 2.54 km (72.9 MPa) (Table 7-8). Depths of crystallization for 68.2% of samples fall in a range 0.63–4.45 km (Table 7-8). The data are evenly distributed between 0 and 6.33 km in the plot of pressure/depth vs MgO (Figure 19). The frequency distribution shows fewer differences among classes from 0 to 5 km than do samples from subaerial Kilauea (Figure 21). The dataset for Puna Ridge (33) is smaller to that for subaerial Kilauea (405), and only a few samples yielded negative pressures that were corrected to 0.1 MPa (depth 0 km). However, the range for the depth of crystallization of the majority of samples from Puna Ridge agrees well with that of samples from subaerial Kilauea. The maximum depth is 6.33 km (181.8 MPa), lower than that for subaerial Kilauea.

The results for Mauna Kea show a very similar range and distribution of depth of crystallization as Kilauea. The average depth is 1.84 km (52.8 MPa), and the greatest depth is 12.6 km (360.63 MPa) (Table 7-8), lower than that of Kilauea. The estimated range of depth of crystallization for 68.2% of the samples (0–4.92 km) is slightly wider than that of Kilauea (Table 7-8). On plot of pressure/depth vs MgO, the data form a cluster over the total depth range (0 to 12.56 km) but the density of data is higher in the range 0 km to 5 km than in the range 5-12.6 km (Figure 19). The histogram showing the distribution of depths is similar to that for Kilauea, with the frequency for each class successively decreasing from 0 to 13 km (Figure 21). The classes with high frequency are those of 0-1 km, 1-2 km, and 2-3 km, with frequencies of 294, 26, and 25 samples, respectively, and ~78% data fall in the range 0-3 km.

A lower range of depths is shown by samples from Mauna Loa than by samples from Kilauea and Mauna Kea (Table, 7-8; Figure 19 & 21). The average depth of samples is 1.49 km (42.8 MPa), whereas the greatest depth is 8 km (22.9 MPa). The estimated range of depth for the majority (~68.2%) of samples is 0–3.58 km. In the plot of pressure/depth vs MgO, the data cluster together over the whole range from the lowest to highest depth (Figure 19). In the

histogram, the frequencies generally decrease among the classes over range from 0–8 km, while the frequency of class 7–8 km is higher than the frequency of classes in the range 4–7 km. And >70% samples fall in the range from 0 to 2 km (Figure 21).

The results for Loi'hi show different distributions of pressure and depth from the other three shield volcanoes. The average depth is 8.7 km (248.7 MPa), and the greatest depth is 22.1 km (635.1 MPa). The estimated range of depth for the majority (68.2%) of samples is wide, from 3.38 to 13.93 km (Table 7-8). On the plot of pressure/depth vs MgO, the data are relatively evenly distributed from 0 to 22.12 km without any distinct clusters (Figure 19). The histogram (1 km class widths) show four separate depth ranges with high frequency (frequency density >10%), 0–1 km, 5–6 km, 7–9 km, and 11–12 km (Figure 21).

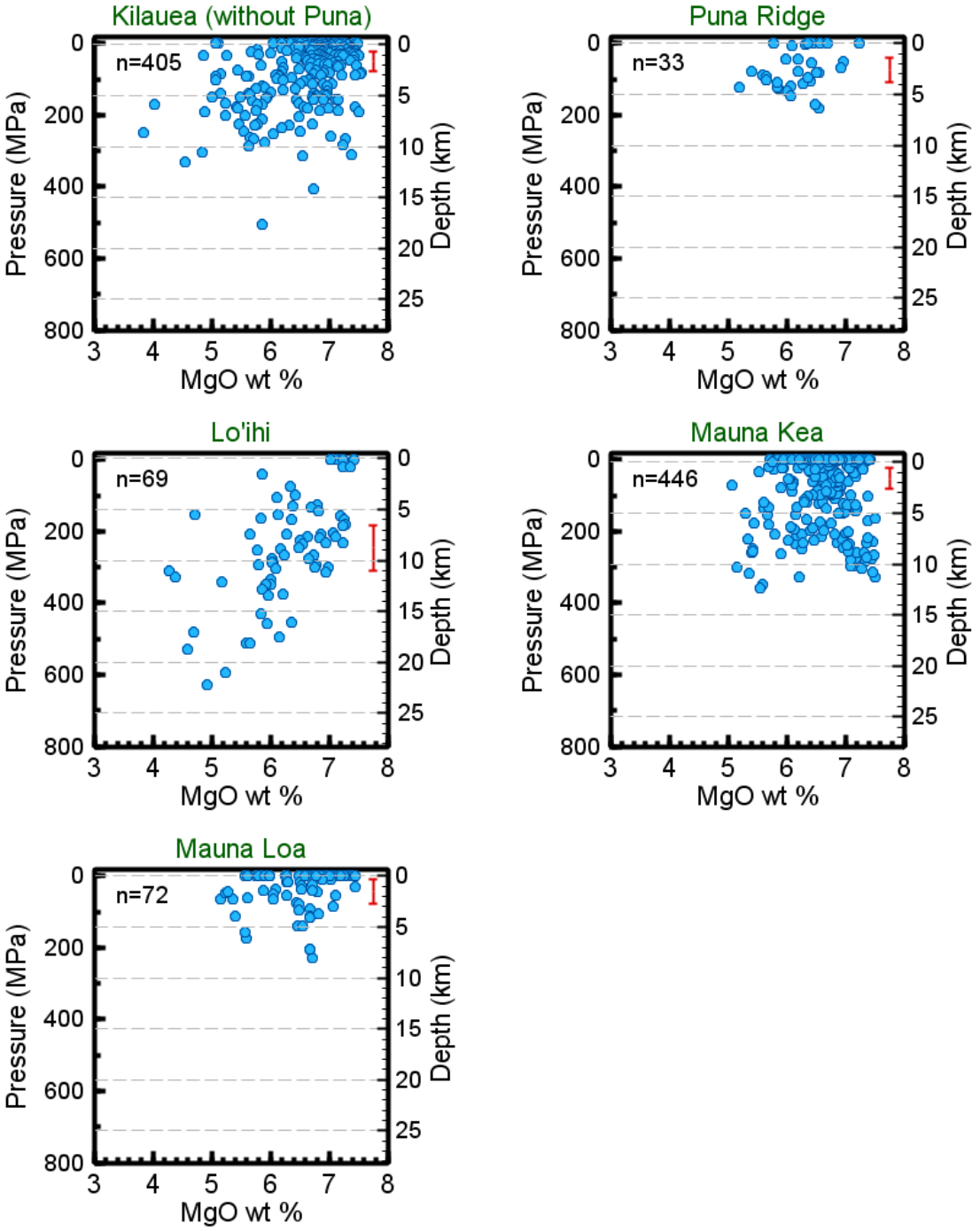

Figure 19. Plots of pressure (P) and Depth (z) vs MgO wt. % using the filtered results of calculated pressure and depth for five locations. The grey dash lines marked based on depth of every 5 km from 0 km. The red segment marked at the top right corner is the error bar that represent the average precision level of the calculation for each location. The center of the error bar is located at the average calculated P and z, while the top and bottom of error bar represent ave P (and z) ± ave error of calculated results of P (and z).

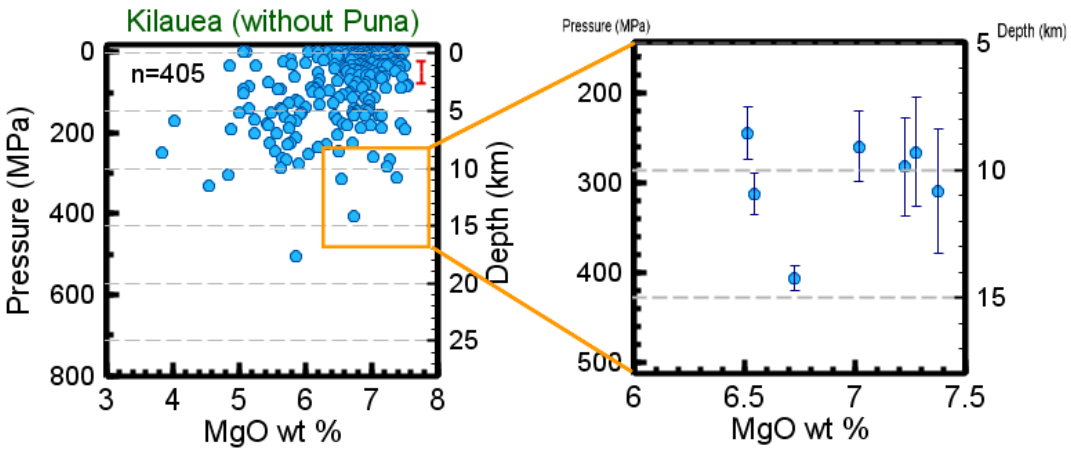

Figure 20. Plots of pressure (P) and Depth (z) vs MgO wt. % of Kilauea (without Puna Ridge). The right plot is a magnification of the area highlighted. The error bars of P (and z) are shown in the right plot, which represent the standard deviation of pressure (and depth) of each sample from six calculated values of pressure (and depth) using the mathematical method by Kelly & Barton (2008). The top and bottom of error bar in right plot, showing the precision of calculation, equals P (and z) ± error of P (and z) of each sample.

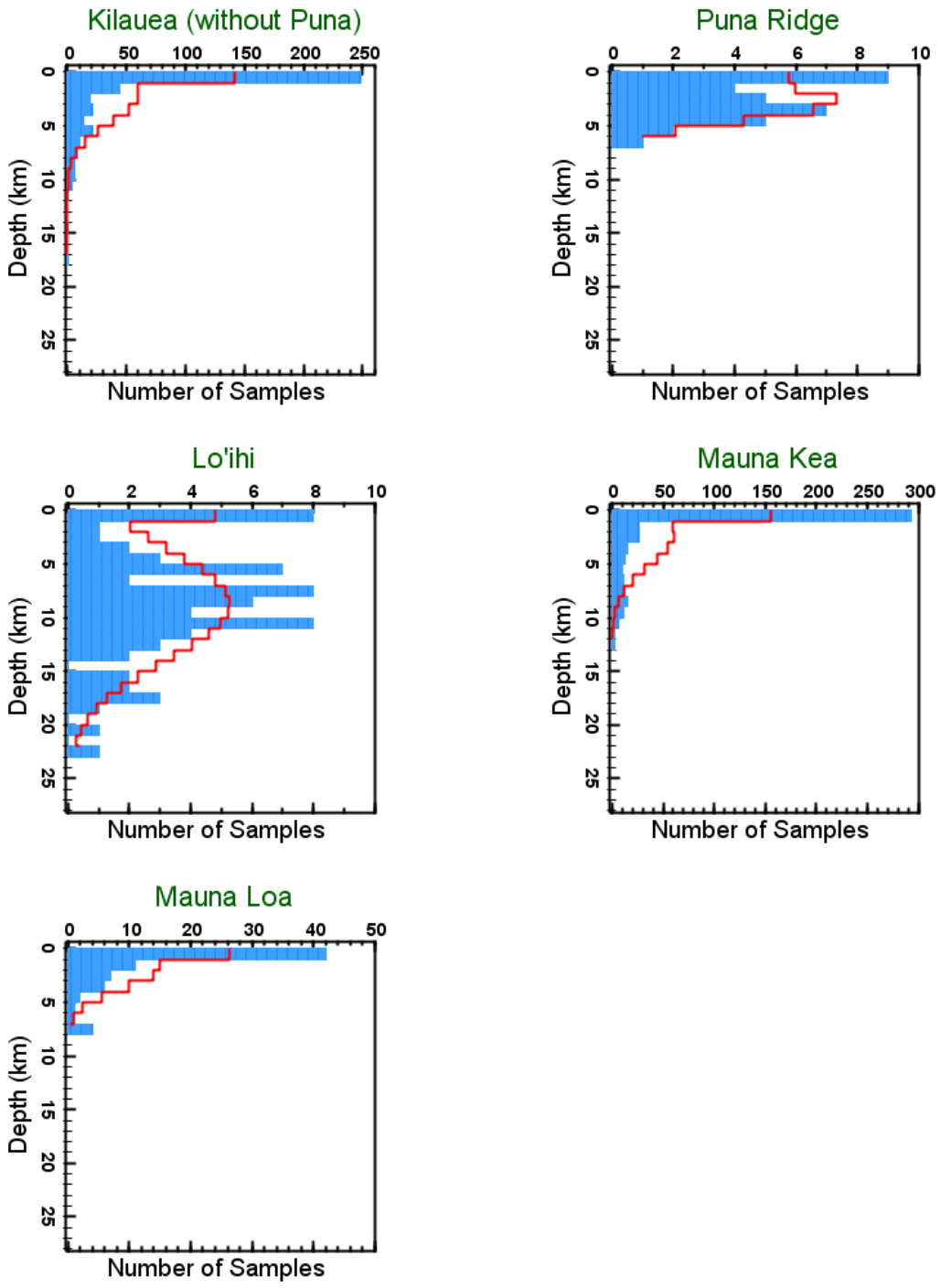

Figure 21. Histogram of calculated depth results for five locations. The red line shows the expected values based on normal distribution. The class width is 1 km for all locations. Direction and scale of depth axis are same as those in Figure 19. Same scale of depth (0–28.15 km) is used for each location.

Table 7. Statistics of calculated pressures for a total number of 1027 samples that have been treated by data filtration by 5 different criteria. In column "Range for 68.2 %...", the range is equal to the average value ± 1 standard deviation of those calculated values of pressure, which means that most samples (about 68.2% assuming the normal distribution) would distribute in this range. In the last column, the average value for all errors of each calculated pressure stand for the average level of precision of pressure calculation for different localities (rows 2–6) and for the overall level of precision in this research (last row). Unit in each column for pressure is MPa.

Volcanoes	Location/ Eruptive Center	Average Pressure	Maximum Pressure	Minimum Pressure	Range for 68.2 % of all results cluster around (Ave P ± 1 σ)	Average Error of Calculated Pressures
Kilauea	*Total Number without Puna (subaerial)	50.8	503.1	0.1	0-130.6	±28.4
	Puna Ridge	72.9	181.7	0.1	18.1-127.8	±34.3
Mauna Kea		52.8	360.2	0.1	0-123.2	±28.8
Mauna Loa		42.8	228.8	0.1	0-102.8	±33.9
Loi'hi		248.7	635.1	0.1	97.0-400.0	±63.0
Total			635.1	0.1		±31.5

Table 8. Statistics of calculated depths for a total number of 1027 samples that have been treated by data filtration by 5 different criteria. In "Range for 68.2 %...", the range is equal to the average value ± 1 standard deviation of those calculated values of depth, which means that most samples (about 68.2% assuming the normal distribution) would distribute in this range. In the last column, the average value for all errors of each calculated depth stand for the average level of precision of depth calculation for different localities (row 2-6) and for the overall level of precision in this research (last row). Unit in each column for depth is km.

Volcanoes	Location/ Eruptive Center	Average Depth	Maximum Depth	Minimum Depth	Range for 68.2 % of all results cluster around (Ave z ± 1 σ)	Average Error of Calculated Depths
Kilauea	*Total Number without Puna (subaerial)	1.77	17.70	0	0-4.55	±0.99
	Puna Ridge	2.54	6.33	0	0.63-4.45	±1.21
Mauna Kea		1.84	12.56	0	0-4.92	±1.01
Mauna Loa		1.49	7.79	0	0-3.58	±1.19
Loi'hi		8.66	22.12	0	3.38-13.93	±2.22
Total			22.12	0		±1.11

The samples from Kilauea are compiled from a large number of individual vents and eruption centers, and for many of these the locations and year of eruption are known. The results for samples from different eruptive vents and different eruptive events are compared to determine possible differences in depths of magma crystallization beneath different regions on the flank of this volcano from the summit caldera to the Puna Ridge extension. In other words, the goal is to investigate possible changes in the sub-crustal distribution of magma from the summit to the east. The results obtained for the depths of crystallization for samples from eight different eruptive centers are shown on plots of pressure/depth vs MgO (Figure 22).

The number of filtered results for both Pu'u'O'o and the Puna Ridge is large, whereas results for a smaller number of samples are available for the other eruptive centers. The distribution of samples from the summit, from Pu'u'O'o, and from Puna Ridge (Figure 22) agree very with the results obtained for samples from sub-aerial Kilauea that were described in a preceding paragraph. The majority of results fall in the range 0-5 km. Two results for samples from Pu'u'O'o indicate crystallization at greater depths, ~9 km and ~11 km. The samples from Makaopuhi Lava Lake range from 5 to 7 km, whereas for the east rift zone (ERZ), the range of depth is~4-11 km for the 1955 late eruption. ERZ samples from 1960 eruption include early, late and those undivided by a specific eruption time and these 22 samples show an even distribution from 0 to 8 km, although the 1960 late samples generally record a shallower depth but higher MgO contents than 1960 early samples. The depth range and MgO contents of 1960 early samples are similar to those of 1955 late samples, which could a migration of magma from a deeper to shallower level over time (from 1955 late to 1960 late). It is also possible that the lack of samples for Makaopuhi, late 1955, and early 1960 provides an incomplete picture of the crystallization history of magmas erupted from these centers because datasets with large numbers of samples such as Pu'u'O'o and Puna Ridge agree much better with the overall characteristics of depth distribution of Kilauea samples with many samples recording crystallization at ~0 km.

The maximum, minimum, and average pressure and depth for each eruptive center on Kilauea are plotted in Figure 23, and these values and statistics are summarized in Table 9. The maximum and minimum values of depth are plotted for each eruptive center instead of the 1σ deviation from the average value because of the small size of the datasets. The depth range of 1960 undivided samples is plotted between the locations of 1960 early and 1960 late samples, but its position does not necessarily indicate that the samples erupted from an intermediate location. The average depth of each eruptive center is within the range of 0-6 km. Pu'u'O'o has a very shallow average value of depth, ~0 km, which is due to the large amount of samples that crystallized very close to the surface (0 km or 0.1 MPa), including samples that initially yielded negative pressures between 0 and -126 MPa that were adjusted to 0.1 MPa. Results for samples from Pu'u'O'o constitute a large proportion of the total number of samples in the filtered subaerial Kilauea database (274 out of 405) so it is not surprising that subaerial Kilauea and Pu'u'O'o samples show a similar depth distribution. Generally, there is no evidence for a significant change in the depth of partial crystallization from the summit caldera to the Puna Ridge.

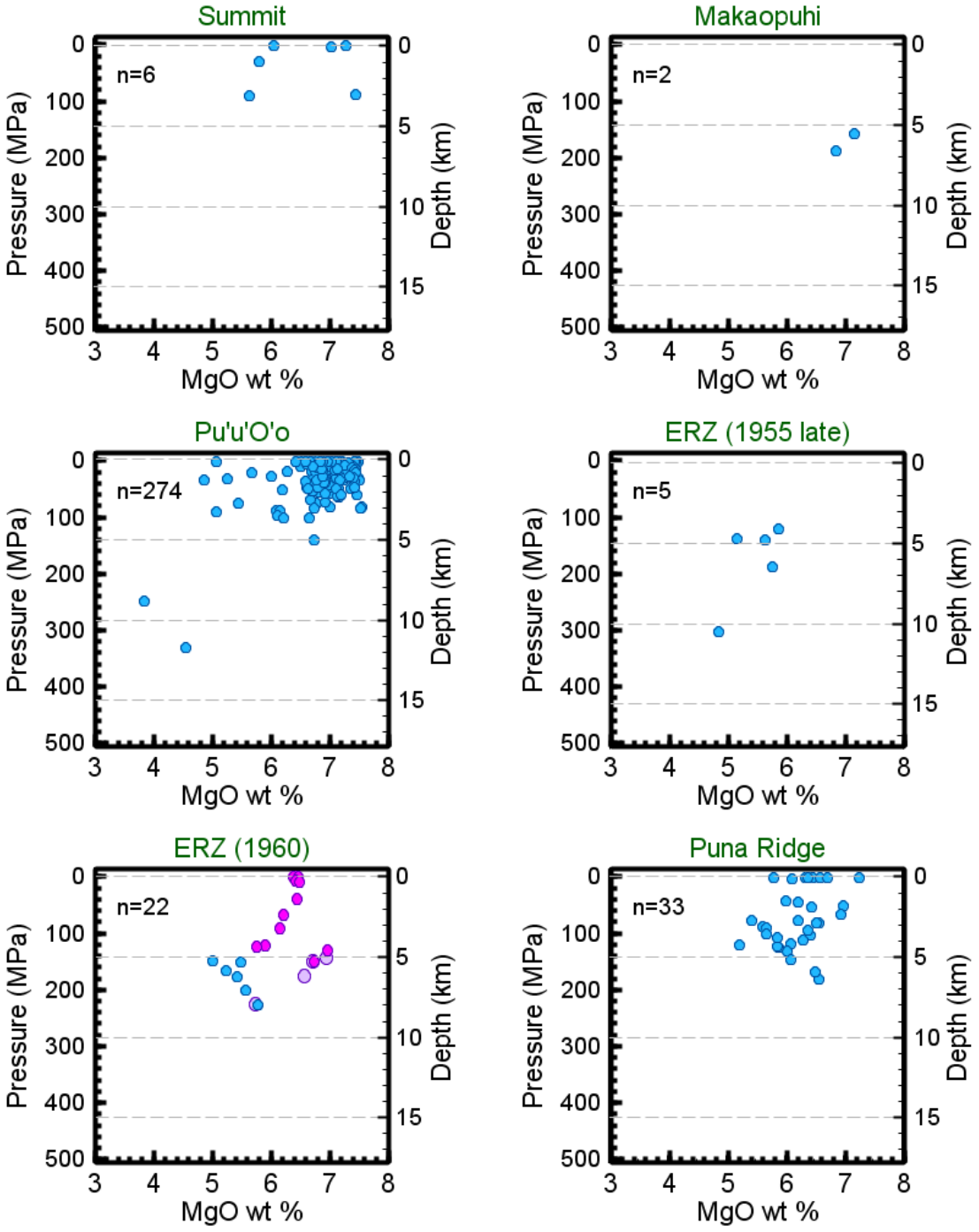

Figure 22. Plots of pressure (P) and Depth (z) vs MgO wt. % using the filtered results of calculated pressure and depth for different locations of Kilauea. The datasets are sorted by location from summit to Puna Ridge (from west to east). The grey dash lines marked every 5 km from 0 km for depth. The total number of data of each location is shown. "ERZ" represent the east rift zone. In "ERZ (1960)", samples in blue are from 1960 early eruption (n=6), samples in magenta are from 1960 late eruption (n=12), and samples in light purple are undivided samples from 1960 eruption (n=4). Scale of depth (0-18 km) is based on the depth range of Kilauea samples (0-17.7 km).

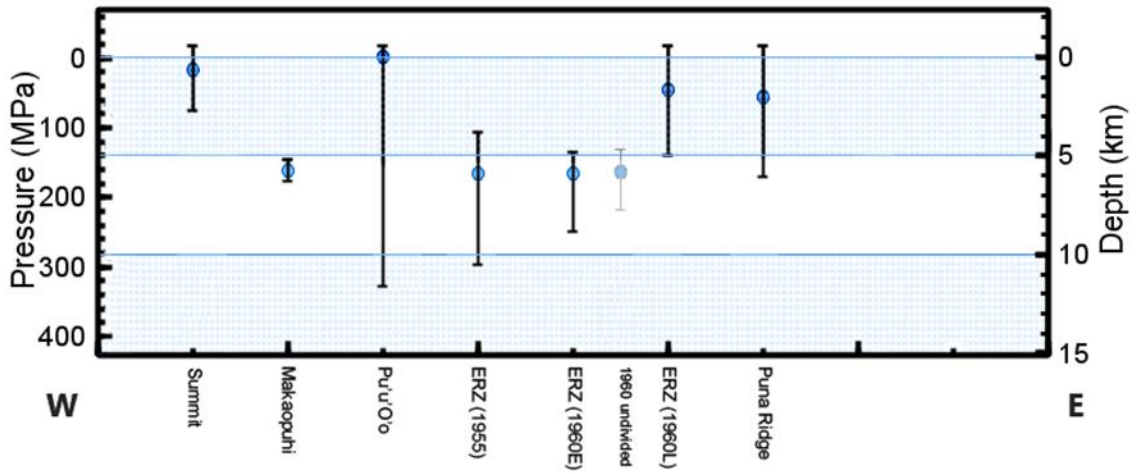

Figure 23. Results of calculated pressure and depth of samples from various eruptive centers/areas of Kilauea. The locations are sorted by direction (west to east), from summit to east rift zone (ERZ) to Puna Ridge. "1960 E" and "1960 L" represent lava of 1960 early eruption and 1960 late eruption. The result of undivided samples from 1960 is plotted in the middle of 1960 early and 1960 late. The time of eruption for samples from each location can be found in Table 9. The blue circles represent the average P (and z) of samples from each location, while the top and bottom of the black segments represent the minimum P (and z) and the maximum P (and z). Average, minimum, and maximum P (and z) are taken from the filtered dataset of results of each location. The specific numbers of these results are shown in Table 9.

Table 9. The statistics (average, maximum, minimum) of calculated pressures and depths for samples that are recorded with specific eruptive centers/area of eruption and eruptive time collected from Kilauea Volcano. These results have been treated by data filtration by 5 different criteria. In row 9, samples of "ERZ (1960)" include the samples from 1960 early eruption (row 6), 1960 late eruption (row 7), and those from 1960 eruption with unknown specific dates (row 8). Unit in each column for pressure is MPa while unit for depth is km.

Location/Eruptive Center	Average Pressure	Maximum Pressure	Minimum Pressure	Average Depth	Maximum Depth	Minimum Depth
Summit (Halema'uma'u Crater and Haiika Crater 1967-1968; 1959 Summit Eruption)	35.0	89.7	0.1	1.23	3.15	0
Makaopuhi lava lake	172.5	187.7	157.4	6.07	6.60	5.54
Pu'u'o'o (1994-1998)	16.7	331.5	0.1	0.59	11.66	0
East Rift Zone (1955 late)	177.2	302.0	119.7	6.24	10.63	4.21
East Rift Zone (1960 early)	177.5	225.7	148.0	6.25	7.94	5.21
East Rift Zone (1960 late)	62.1	151.0	0.1	2.91	5.31	0
East Rift Zone (1960 undivided)	174.3	226.2	144.0	6.13	7.96	5.07
Puna Ridge	72.9	181.7	0.1	2.54	6.33	0

Interpretation of Magma Plumbing Systems

The structure of the magma plumbing system can be constructed from the depths of partial crystallization calculated from glass analyses, taking into account the errors associated with the calculations. However, it is important to consider also the results obtained using other methods (GPS, seismology) to obtain a consistent model for the plumbing system beneath Hawaiian volcanoes.

Kilauea

Kilauea has been nearly continuously erupting since 1983 (Heliker et al., 2003) and the magma plumbing system of Kilauea is well understood by ongoing geophysical and petrologic studies. Detailed geophysical studies have been carried out by several workers for Kilauea, and one of the best known is that by Ryan et al. (1981). In that work, these workers, based on analysis of seismic data, concluded that the primary conduit transports magma from 14.6 km (mantle) to 6.5 km (effective floor of summit storage complex) beneath the Kilauea summit and a cylindrical region transports magma from a depth of 5.7 km to 1.9 km beneath the east rift zone. This model is followed by the seismic study by Ryan (1988) in which he presented an interpretation of the three-dimensional magma plumbing system (Figure 24): a large sub-caldera magma reservoir was inferred to exist at 2–4 km, a primary conduit extending to depths of ~34 km within upper mantle that fed magma into the shallow reservoir, and wholly molten rift zones that occupied depth of 3-10 km.

The depth of magma reservoir beneath the summit caldera (2–3 km) is estimated from 1967–1968 Halema'uma'u tilt data by Fiske & Kinoshita (1969). Klein (1982) noted that eruptions are accompanied by ground deformation, and determined that the depth of the magma reservoir as 2–3 km beneath the caldera. Dzurisin et al. (1984) inferred a depth of 2–6 km beneath the summit for the magma reservoir, whereas the results of the seismic study by Wright & Klein (2006) led to identification of the shallow magma reservoir at a depth of 4–6 km beneath the summit with magma transported along a roughly cylindrical conduit from the melting source at 80–100 km depth in the asthenosphere, with a location error ±2 km (2σ). The depth of clusters of volume changes beneath the summit and southwest rift zone identified by InSAR in Zhai & Shirzaei (2016) indicated the magma storage zone beneath summit is located in range of 1–6 km, including the active sources with volume change with 1–4 km. The shallow magma reservoir was modeled as a single-point source (< 3.5 km) by GPS observations (Cervelli & Miklius, 2003).

Several other geophysical studies have indicated that there are two long-term, interconnected magma bodies beneath the summit caldera, termed as the Halema'uma'u reservoir and the south caldera reservoir (~3 km and ~1 km, respectively) by Poland et al. (2014). The former one, located at the east margin of Halema'uma'u, the depth is interpreted as ~1 km by Almendros et al. (2002) 1–2 km by Poland et al. (2009), and ~1.4 km by Lundgren et al. (2013). A seismic study by Dawson et al. (1999) identified two reservoirs within depths of 1–4 km beneath the southeast portion of the caldera, and the one ~1 km agrees with the location of Halema'uma'u reservoir. The south caldera reservoir, however, is interpreted as a spherical reservoir that is located at 2.9 km by Poland et al. (2012), and at a depth of 3 km by Wauthier et al. (2016). The depth of the sill beneath the southwest rift zone interconnected with the south caldera reservoir is estimated at ~3 km (Okada, 1985; Wauthier et al., 2016).

Petrologic studies have also debated the structure of shallow magma reservoirs beneath the summit caldera. Major and trace element whole-rock data and the isotopic ratio of lavas indicate a single spherical magma reservoir beneath the summit (Pietruszka and Garcia, 1999). However, a later geochemical study using Pb isotopes indicates that two magma bodies are beneath the summit, including the one beneath the southern rim of summit caldera is located at depth ~2–4 km and the another beneath eastern rim of Halema'uma'u crater (<2 km) (Pietruszka et al., 2015). They also indicated that the summit reservoir formed the structure with two magma bodies since at least 1971 and probably since 1959.

Two rift zones of Kilauea, the east rift zone (ERZ) and the southwest rift zone (SWRZ), comprise a series of eruptive vents (Poland et al., 2014). The seismic study by Wright & Klein (2006) revealed that magma transports nearly vertically to the shallow summit reservoir from 20 km beneath the summit caldera and then transports laterally into the ERZ at a depth ~5 km from the shallow summit reservoir. Magma that is supplied for intrusions and extrusions is stored in a region 4–7 km beneath the ERZ (Wright & Klein, 2006). A molten core beneath the ERZ connects the summit to the distal subaerial end of the rift zone (~50 km for plan view) and probably even into the submarine part (Puna Ridge) (Fiske et al., 1993). The ERZ molten core interpreted by Johnson (1995b) is at 3–5 km depth. Several geophysical studies interpreted that the magma transport beneath ERZ connected to the south caldera reservoir is at a depth of ~ 3 km (Klein et al., 1987; Wolfe et al., 1987; Lundgren et al., 2013). While some studies suggested that magma flows through the south caldera reservoir into ERZ without time for magma storage and eruption (for example, gravity study by Johnson, 1987), other studies indicate that magma also stored at a shallow region of the ERZ. For example, a reservoir beneath Makaopuhi Crater is identified by seismic and deformation data (Jackson et al., 1975; Swanson et al., 1976) while a reservoir near Makaopuhi is projected by several other studies (Wolfe et al., 1987; Owen et al., 2000; Segall et al., 2001). The reservoir beneath Pu'u'O'o is interrelated by geophysical data (Hoffman et al., 1990; Owen et al., 2000; Segall et al., 2001) and petrologic data (Garcia et al., 1992). Petrologic study on lavas from 1955 and 1966 ERZ eruption suggested that both eruptions experienced magma mixing between evolved magmas stored in the ERZ and primitive magmas from the summit reservoir (Helz and Wright, 1992; Wright and Helz, 1996).

Magmas storage and transport at deep rift zones has also proposed by geophysical and petrologic studies. Presence of melt from ~3 km to 9 km has been recognized by deformation data (Dieterich, 1988; Owen et al., 2000). The magma storage (~8–11 km) at nearly the base of volcanic pile beneath east rift zone is indicated by anomalous seismic velocity (Lin et al., 2014). Gravity data indicate dense intrusions that extend from the base of volcanic pile (Kauahikaua et al., 2000). Petrologic evidence suggests that magma in the ERZ eruptions are fed by magma that rises from a deep rift zone connected to lower summit region without passing through the summit magma reservoir (Wright & Helz, 1996; Vinet & Higgins, 2010). The magmas stored at deep region beneath the ERZ are indicated by olivine compositions (Vinet & Higgins, 2010; Helz et al., 2014).

In our study, the overall range of depths (0–11 km) estimated by glass analyses of samples from Kilauea reveals excellent agreement with the results from previous studies. The range of depths (0–4.5 km) of majority (including undivided samples) is consistent with the range of depths (~1–5 km) of the summit reservoir estimated by most geophysical work, which indicates that most samples probably erupt from the large reservoir beneath the summit. Based on the majority of samples, there is no gap (lack of samples) at depth of ~2–3 km (Figure 21) in our study in

comparison with the range of depth of proposed Halema'uma'u reservoir (~1–2 km) and the south caldera reservoir (~3–5 km) in some previous studies. The range of depth of samples from summit (0–3.5 km) estimated by samples with recorded eruptive vent (Figure 22), however, seem to lack samples at depth of ~2-3 km, and these samples could erupt from both the shallower Halema'uma'u reservoir and the deeper south caldera reservoir if the proposed model with two reservoirs beneath the summit is correct.

For the results on the ERZ in our study, there could be a molten core including several isolated magma bodies within the range of 0–5 km in the shallow ERZ as the samples form Pu'u'O'o, ERZ 1960 late eruption, and Puna Ridge (Figures 22–23) fall in the range of ~0–5 km, consistent with the molten core (~3–5 km) and sub-horizontal transport between summit and ERZ (~3 km) proposed by previous studies. Our results confirm that magma reservoirs exist beneath Makaopuhi and Pu'u'O'o (Figure 22), and provide an estimate of their depths (~5–7 km and ~0–4 km, respectively). Samples clustered near ~8–11 km (Figure 19) present an excellent agreement with the magma reservoir (~8–11 km) near the base of the volcanic pile beneath the ERZ proposed by seismic studies. Magma reservoirs and the lateral transport within the deep rift zone at depth between ~3 km and base of volcano (~13 km, Hill and Zucca, 1987) could exist, as some samples from each eruptive vent fall within this range in our study (Figures 22–23). Although there are two samples at ~14 km and ~17 km) in our study (Figure 19), as they are not clustered with any other samples, they may not able to indicate magma bodies below the base of volcano. The eruptions along the ERZ could be fed by magmas from reservoirs beneath the ERZ, or magmas from the shallow summit reservoir, or the mixing of both resident magmas and primitive magmas. In addition, the result in our study also revealed the depth (majority within 0.6–4.5 km) of magma reservoirs that supply the eruption of Puna Ridge, consistent with the depth of summit magma reservoir (0–4.5 km). Therefore, the summit magma reservoir could also provide magmas for eruptions in this region.

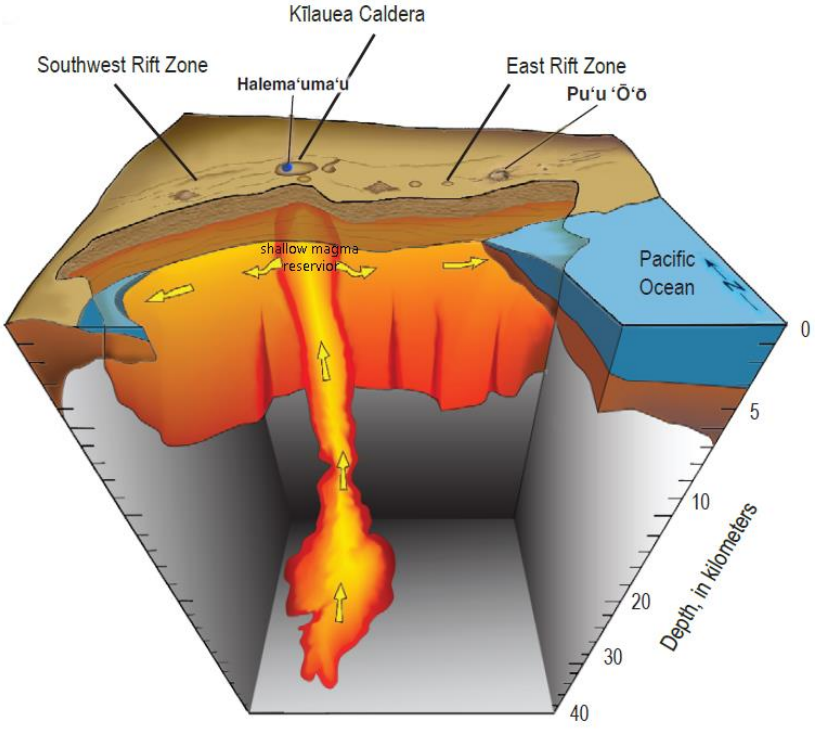

Figure 24. Northward-directed cut view of internal structure of Kilauea, showing shallow magma reservoir beneath the summit caldera, magma pathway of the primary vertical conduit, and the lateral magma transport along a level of 2–4 km beneath the surface. Magma transport is marked by yellow arrows. Model is constructed by Ryan et al. (1981) and Ryan (1988) based on seismicity patterns and subsurface density structure, and simplified by Poland et al. (2014). Modified from Poland et al. (2014).

Mauna Loa

Mauna Loa has exhibited less eruptive activity (only 1975 and 1984 recent eruptions) compared to Kilauea and hence much less geophysical work has been conducted on the magma plumbing system beneath Mauna Loa. Yet, previous geophysical studies reveal that the shallow magma stored at ~3–4 km beneath the summit caldera. For example, a magma chamber about 4 km beneath the southeastern part of the caldera was defined by the seismic study by Decker et al. (1983). Tilt and leveling studies by Johnson (1995a) suggested that magma is stored at 3.5 km beneath the southeast of caldera and coupled with the dike (0–5 km) at the northeast rift zone. The model constructed by InSAR data by Amelung et al. (2007) include a spherical magma body (4.7 km) beneath the southeast margin of the caldera and a dike-like structure (4-8 km) that extend from caldera and through the rift zones. In general, the pattern of subsurface seismicity at Mauna Loa is similar to Kilauea for both summit and rift zones, based on seismic studies (Koyanagi et al, 1987). The monitoring of 1975 and 1984 eruptions indicated that Mauna Loa's plumbing system is similar to Kilauea although the size of magma reservoir beneath Mauna Loa might be larger than that beneath Kilauea (Tilling & Heliker, 2010). And for deep storage of magma, the depth of hypocenters (36–45 km) beneath Mauna Loa summit caldera (Okubo et al., 2014) is approximate the same as where Kilauea's primary conduit beneath the caldera zoned within upper mantle (~34 km) (Ryan et al., 1988).

In our study, the range of depth 0–3.58 km (average=1.49 km) is consistent with the result (3–4 km) in previous studies (for example, Decker et al., 1983, Johnson, 1995b, and Amelung et al., 2007), and indicate that Mauna Loa probably has a similar shallow magma reservoir as Kilauea. But unlike Kilauea, the deeper magma storage (maximum depth=7.79 km) estimated in our study is much shallower than the base of the volcanic pile, ~17 km, (Lipman, 1995) and the thickness of oceanic crust, ~18 km, (Hill and Zucca, 1987) beneath Mauna Loa. Mauna Lao and Kilauea share magma supply from the deeper area (hot spot) and all hot-spot magma degas through Kilauea's summit (Poland et al., 2014), but Mauna Loa probably has its own shallow magma reservoir that is separated from the magma reservoirs beneath Kilauea as seismic data identified two clusters of earthquake associated with magma supply of Kilauea while another cluster located south of Mauna Loa within shallow subsurface area (Wright & Klein, 2006).

Mauna Kea

Mauna Kea, unlike active volcanoes, is considered dormant (Wolfe et al., 1997) and it is unable to get access to geophysical and geodetic studies in recent years, but its plumbing system can still be interpreted by petrologic studies. A petrologic study in Yang et al. (1999) indicates that Mauna Kea may have similar depth of summit reservoir as Kilauea (shallow reservoir at 2–7 km) during its shield building stage, while isolated magma pockets (rarely erupted) may form within the various ranges of depths as a result of decreased omagma supply (Yang et al., 1999). Also, lateral transport of magma from the central vertical conduit into rift zones could occur at depth of boundary of crust and uppermost mantle (~15 km) (Yang et al., 1999). The petrologic study by Clague (1987) reveals that tholeiitic magma is stored in a shallow reservoir (~3–7 km below surface) beneath the summit during the shield stage while alkalic magma is stored in an intermediate magma (20 km) at the crust-mantle boundary during post-shield stage. During the post shield stage, the magma plumbing system changes (shallow chambers and crustal conduits crystallize) because magma supply rate substantially decreases and become insufficient to feed shallow magma chambers (Frey et al., 1991). The illustrations of plumbing system in petrologic study by Frey et al. (1991) show a shallow magma chamber (~3 km above to 2 km below sea level, or 1–6 km beneath surface) with lateral magma transport (~0 km) into the rift zones during late shield stage, and only some collects of magma (below 15 km) during post-shield stage.

The results of our study show that Mauna Kea have range of depth of magma chambers similar to those of Kilauea and hence could have similar structure to those of Kilauea, as the range of depth of most samples (0–4.92 km) and the average depth (1.84 km) indicate that Mauna Kea probably has a shallow reservoir with large volume of magma, and samples at ~10 km indicate magma crystallization also occur ~8–10 km. The result of depth ~0-5 km in our study agrees well with the shallow magma chamber beneath the caldera interpreted in previous petrologic studies. In addition, magma could also be stored at deeper region beneath the Mauna Kea caldera in shield stage as well as Kilauea, given that most samples from Mauna Kea in our study have tholeiitic components (similar to Kilauea) that typically represent the shield stage magma (Figure 6). It is reasonable that Mauna Kea had plumbing system similar to that of Kilauea because Mauna Kea has the characteristics of large shield volcanoes (Kilauea and Mauna Loa) such as its broad summit with indented caldera, although it has less smooth appearance in comparison with Mauna Loa (Tilling & Heliker, 2010). Our interpretation of current plumbing system of Kilauea may provide information for that of Mauna Kea during shield stage, as both of them are on the Kea trend (Figure 3) and considered to be formed by the relatively fixed mantle plume (Tilling & Heliker, 2010).

Lo'ihi

Loi'hi, the youngest volcano in this study, may have same the deep magma supplies as Kilauea and Mauna Loa (Tilling et al., 2010), but there are fewer previous studies of Loi'hi that provided quantitative estimates of depth of magma chambers in comparison to Kilauea and Mauna Loa. In their seismic study Koyanagi et al. (1987) suggested that the clusters of volcanically generated LP (long-period) earthquakes may indicate a magma reservoir at ~15 km. A petrologic study (Garcia et al., 1998) generated a shallower result than the seismic study, which reveals that the tholeiitic lavas erupted in 1996 crystallized at depth (8–9 km) based on the analysis of mineralogy of lavas, although this result also indicated that the magma chamber supplied by intrusion of mafic magma beneath Lo'ihi is deeper than those of the shield volcanoes.

The results of our study, however, give a much wider range of depths (0–22.12 km) with a more scattered distribution than in previous studies. The average depth (8.66 km) and one of the ranges of relatively high frequency density (>10%) of samples (7–9 km) in our study agree well with the results in a petrologic study by Garcia et al. (1998). Another range of depths with high frequency density (>10%) of samples, 11–12 km, in our study is consistent with the results (~15 km) of a seismic study by Koyanagi et al. (1987) if the errors are taken into account. Shallower depth ranges (i.e., 0–1 km and 5–6 km) estimated by our method could still indicate magma reservoirs, because a magma source with aseismic transport is also possibly located (Wright & Klein, 2006) beneath Loi'hi. Generally, the highly scattered distribution of depths, which is different from the result of the shield volcanoes, indicates that the plumbing system of Loi'hi is currently not fully developed as Lo'ihi still experience its transition between pre-shield to shield stage.

CONCLUSIONS

A petrologic method to calculate the pressure of partial crystallization of melts lying along the ol-plag-cpx cotectic based on the method described by Kelly & Barton (2008) has been used to estimate the depth of magma chambers beneath Hawaiian volcanoes. The major element compositions of basalt glasses are used as input data because glass represents the quenched melts of pre-eruption magma compositions and the method of calculation is calibrated for basalt. The combined upper limit of accuracy and precision of the method is 126 MPa, but the error in the calculated pressure for most samples in this study is 28–34 Mpa. Chemical compositions, especially CaO, Al_2O_3 and MgO contents, are used to identify the liquid compositions in equilibrium with ol-plag-cpx and to distinguish these from liquids in equilibrium with only ol. Chemical variations are also used to infer models of magma evolution and hence to constrain different interpretations (i.e., mixing, assimilation, and polybaric crystallization of calculated pressures of partial crystallization. Olivine-hosted glass inclusions lying on the trend of iron-enrichment can also be used as input data, but those affected by Fe-Mg exchange are not appropriate for use.

The majority of the results falls in the depth range of 0–4.9 km (0–139 MPa) for the three shield volcanoes, although the depths obtained for Mauna Loa are generally lower than those obtained for Mauna Kea and Kilauea. Both Mauna Kea and Kilauea have some glasses that crystallize at ~11 km, a depth equivalent to the base of the volcanic pile and close to the base of the crust beneath these volcanoes. The depth for glasses from the Puna Ridge (0.63–4.45 km) is approximately the same as for the majority of samples from Kilauea (0–4.55 km), which is consistent with Puna Ridge being an extension of the east rift zone of Kilauea. Also, eruptive centers along the east rift zone of Kilauea (from west to east) show no clear systematic differences in the range of depth of partial crystallization. Magmas beneath Lo'ihi crystallized at a higher average depth and over a wider range of depths than beneath the other shield volcanoes, which suggests that the plumbing system beneath Lo'ihi is not yet fully developed. The estimated depths of magma reservoirs agree well with the depths estimated with other methods. Hawaiian volcanic plumbing systems evolve over time as the result of Pacific Plate motion over the hot spot, and Lo'ihi, lying along the Loa trend, will probably develop a plumbing system similar to that of Mauna Loa when it reaches shield stage in the future.

RECOMMENDATIONS FOR FUTURE WORK

More glass analysis of the lava and hyaloclastite samples and compilation of datasets based on a series of location and time for each volcano on the Big island of Hawaii could provide more information for interpreting the structure of the plumbing system. As this research has done some comparison of different eruptive centers of Kilauea (roughly along west-east line) with the information of samples that we have, a better comparison could be conducted by including additional samples from localities (e.g., along a line of same latitude) and eruption years (e.g., 1950s, 1960s and 1980s) for Kilauea and other volcanoes. This requires analysis works of additional samples that have been collected from known eruption centers and defined with respect to age of eruptive event. Calculation of the pressures and depths for these samples would provide information about the location of magma bodies beneath each volcano allowing a more detailed picture of the plumbing system to be drawn.

Another possibility is to take the effect of H_2O into consideration, as the calculations reported in this work are based on the assumption of anhydrous conditions. Calculation of pressures using different magmatic water contents using petrologic methods is necessary to determine if the calculated pressures will be significantly affected by additional water. Analysis of samples to determine the H_2O content will allow more accurate pressures of partial crystallization if additional datasets are obtained.

In addition, more exact pressures can be estimated if the calculated pressures of submarine samples in this research are corrected for the water column depth. This will affect the pressures calculated for samples from Lo'ihi (top of seamount is approximately 975 m below sea level) and Kilauea's submarine extension, Puna Ridge. The pressure exerted by the water column for these localities could be calculated and removed if there was information about the depth for the collection of each sample. However, although more accurate estimates of pressure would be obtained, the effect of the water column should be relatively small given the shallow water depths around Hawaii.

REFERENCES CITED

Abouchami, W., Hofmann, A.W., Galer, S.J.G., Frey, F.A., Eisele, J., and Feigenson, M., 2005, Lead isotopes reveal bilateral asymmetry and vertical continuity in the Hawaiian mantle plume: Nature, v. 434, p. 851–856.

Amelung, F., Yun, S. H., Walter, T.R., Segall, P., and Kim, S.-W., 2007, Stress control of deep rift intrusion at Mauna Loa volcano, Hawaii: Science, v. 316, no. 5827, p. 1026–1030.

Almendros, J., Chouet, B., and Dawson, P., 2001, Spatial extent of a hydrothermal system at Kilauea Volcano, Hawaii, determined from array analyses of shallow long-period seismicity; 2. Results: Journal of Geophysical Research, v. 106,

Becerril, L., Galindo, I., Gudmundsson, A., & Morales, J. M., 2013, Depth of origin of magma in eruptions: Scientific Reports, v. 3, p. 2762.

Cervelli, P.F., Miklius, A., 2003, The shallow magmatic system of Kilauea Volcano. In: Pu`u `O`o–Kupaianaha Eruption of Kilauea Volcano, Hawai`i First 20 Years, p. 149–164.

Clague, D.A., 1987, Hawaiian xenolith populations, magma supply rates, and development of magma chambers: Bulletin of Volcanology, v. 49, p. 577–587

Clague, D., Moore, J., Dixon, J., and Friesen, W., 1995, Petrology of Submarine Lavas from Kilauea's Puna Ridge, Hawaii: Journal of Petrology, v. 36, p. 299-349

Clague, D.A. and Dalrymple, G.B., 1987, The Hawaiian-Emperor volcanic chain. part I. Geologic evolution: Volcanism in Hawaii, v. 1, p. 5-54.

Clague, D.A., unpublished.

Danyushevsky, L.V., McNeill, A.W., and Sobolev, A.V., 2002, Experimental and petrological studies of melt inclusions in phenocrysts from mantle-derived magmas: an overview of techniques, advantages and complications: Chemical Geology, v. 183, p. 5–24.

Davis, M.G., Garcia, M.O., and Wallace P., 2003, Volatiles in glasses from Mauna Loa Volcano, Hawaii: implications for magma degassing and contamination, and growth of Hawaiian volcanoes: Contrib. Mineral Petrol. v. 144, p. 570-591.

Dawson, P.B., Chouet, B.A., Okubo, P.G., Villasenor, A., and Benz, H.M., 1999, Three-dimensional velocity structure of the Kilauea caldera, Hawaii: Geophysical Research Letters, v. 26, p. 2805–2808.

Decker, R.W., Koyanagi, R.Y., Dvorak, J.J., Lockwood, J.P., Okamura, A.T., Yamashita, K.M. and Tanigawa, W.R., 1983, Seismicity and surface deformation of Mauna Loa volcano, Hawaii: Eos, Transactions American Geophysical Union, v. 64, p.545-547.

Dieterich, J.H., 1988, Growth and persistence of Hawaiian volcanic rift zones: Journal of Geophysical Research, v. 93, no. B5, p. 4258–4270.

Dzurisin, D., Koyanagi, R.Y., and English, T.T., 1984, Magma supply and storage at Kilauea volcano, Hawaii, 1956–1983: Journal of Volcanology and Geothermal Research, v. 21, p. 177–206.

Fiske, R.S., and Kinoshita, W.T., 1969, Inflation of Kilauea Volcano Prior to Its 1967-1968 Eruption: Science, v. 165, p. 341–349.

Fiske, R.S., Swanson, D.A., and Wright, T.L., 1993, A model of Kilauea Volcano's rift-zone magma system [abs.]: Eos (American Geophysical Union Transactions), v. 74, no. 43, supp., p. 646, abstract no. V22F–5.

Frey, F.A., Garcia, M.O., Wise, W.S., Kennedy, A., Gurriet, P., and Albarede, F., 1991, The evolution of Mauna Kea volcano, Hawaii: Petrogenesis of tholeiitic and alkalic basalts: Journal of Geophysical Research, v. 96, p. 14,347–14,375.

Frey, F.A., Huang, S., Xu, G., and Jochum, K.P., 2016, The geochemical components that distinguish Loa- and Kea-trend Hawaiian shield lavas: Geochimica et Cosmochimica Acta, v. 185, p. 160–181.

Furumoto, A.S., Woollard, G.P., Campbell, J.F. and Hussong, D.M., 1968, Variation in the thickness of the crust in the Hawaiian Archipelago: The Crust and Upper Mantle of the Pacific Area, p.94-111.

Garcia, M.O., Muenow, D.W., Aggrey, K.E., and O'Neil, J.R., 1989, Major element, volatile, and stable isotope geochemistry of Hawaiian submarine tholeiitic glasses: Journal of Geophysical Research: Solid Earth, v. 94, p. 10525–10538.

Garcia, M.O., Rhodes, J.M., Wolfe, E.W., Ulrich, G.E., and Ho, R.A., 1992, Petrology of lavas from episodes 2–47 of the Puu Oo eruption of Kilauea Volcano, Hawaii; evaluation of magmatic processes: Bulletin of Volcanology, v. 55, nos. 1–2, p. 1–16.

Garcia, M.O., Rubin, K.H., Norman, M.D., Rhodes, J.M., Graham, D.W., Muenow, D.W., and Spencer, K., 1998, Petrology and geochronology of basalt breccia from the 1996 earthquake swarm of Loihi seamount, Hawaii: magmatic history of its 1996 eruption: Bulletin of Volcanology, v. 59, p. 577–592.

Hanano, D., Weis, D., Aciego, S., Scoates, J.S. and DePaolo, D.J., Geochemistry of post-shield lavas from paired Loa-and Kea-trend Hawaiian volcanoes: Geochimica et Cosmochimica Acta 2007, Abstracts, v. 71, no. 15, p. A375-A375.

Hawkins, J., and Melchior, J., 1983, Petrology of basalts from Loihi Seamount, Hawaii: Earth and Planetary Science Letters, v. 66, p. 356–368.

Heliker, C., Swanson, D.A., and Takahashi, T.J., 2003, The Pu'u 'O'o-Kupaianaha eruption of Kilauea volcano, Hawai'i: the first 20 years: Reston, U.S. Geological Survey, p. 215.

Helz, R.T., Clague, D.A., Sisson, T.W., and Thornber, C.R., 2014, Petrologic insights into basaltic volcanism, chap. 6 of Poland, M.P., Takahashi, T.J., and Landowski, C.M.,eds., Characteristics of Hawaiian volcanoes: U.S. Geological Survey Professional Paper 1801.

Helz, R.T. and Wright, T.L., 1992, Differentiation and Magma Mixing on Kilauea's East Rift Zone: Bulletin of Volcanology, v. 54, p. 361-384.

Helz, R.T. and Wright, T.L., 1996, Differentiation and Magma Mixing on Kilauea's East Rift Zone: A further look at the eruptions of 1955 and 1960. Part II. The 1960 lavas: Bulletin of Volcanology, v. 57, p. 602-630.

Herzberg, C., 2004, Partial crystallization of mid-ocean ridge basalts in the crust and mantle: Journal of Petrology, v. 45, p. 2389-2405.

Hill, D.P., Zucca, J.J., 1987, Geophysical constraints on the structure of Kilauea and Mauna Loa Volcanoes and some implications for seismomagmatic processes. In: Decker, R.W., Wright, T.L., Stauffer, P.H. (Eds.), Volcanism in Hawaii, 2 V, U.S. Geological Survey Professional Paper, v. 1350(2), p. 903– 917. chap 37.

Hofmann, A.W., and Farnetani, C.G., 2013, Two views of Hawaiian plume structure: Geochemistry, Geophysics, Geosystems, v. 14, p. 5308–5322.

Jackson, D.B., Swanson, D.A., Koyanagi, R.Y., and Wright, T.L., 1975, The August and October 1968 east rift eruptions of Kilauea Volcano, Hawaii: U.S. Geological Survey Professional Paper 890, 33 p.

Johnson, D.J., 1987, Elastic and inelastic magma storage at Kilauea Volcano, chap. 47 of Decker, R.W., Wright, T.L., and Stauffer, P.H., eds., Volcanism in Hawaii: U.S. Geological Survey Professional Paper 1350, v. 2, p. 1297–1306.

Johnson, D.J., 1995a, Gravity changes on Mauna Loa volcano, in Rhodes, J.M., and Lockwood, J.P., eds., Mauna Loa revealed; structure, composition, history, and hazards: American Geophysical Union Geophysical Monograph 92, p. 127–143.

Johnson, D.J., 1995b, Molten core model for Hawaiian rift zones: Journal of Volcanology and Geothermal Research, v. 66, nos. 1–4, p. 27–35.

Kauahikaua, J., Hildenbrand, T., and Webring, M., 2000, Deep magmatic structures of Hawaiian volcanoes, imaged by three-dimensional gravity methods: Geology, v. 28, no. 10, p. 883–886.

Kelley, D. F. & Barton, M., 2008, Pressures of Crystallization of Icelandic magmas, Journal of Petrology, v. 49(3), p. 465-492.

Klein, F.W., 1982, Patterns of historical eruptions at Hawaiian volcanoes: Journal of Volcanology and Geothermal Research, v. 12, nos. 1–2, p. 1–35.

Klein, F.W., Koyanagi, R.Y., Nakata, J.S., and Tanigawa, W.R., 1987, The seismicity of Kilauea's magma system, chap. 43 of Decker, R.W., Wright, T.L., and Stauffer, P.H., eds., Volcanism in Hawaii: U.S. Geological Survey Professional Paper 1350, v. 2, p. 1019–1185.

Koyanagi, R.Y., Chouet, B. and Aki, K., 1987. Origin of volcanic tremor in Hawaii: Part I. Data from the Hawaiian Volcano Observatory,1969-1985. In: Decker, R.W., Wright, T.L., Stauffer, P.H. eds., Volcanism in Hawaii, 2 V: U.S. Geological Survey Professional Paper, v. 1350(2), p. 1221–1257. chap. 45.

Laubier, M., Schiano, P., Doucelance, R., Ottolini, L., and Laporte, D., 2007, Olivine-hosted melt inclusions and melting processes beneath the FAMOUS zone (Mid-Atlantic Ridge): Chemical Geology, v. 240, p. 129–150.

Le Bas, M. J., Le Maitre, R.W., Streckeisen, A. & Zanettin, B., 1986, A chemical classification of volcanic rocks based on the total alkalisilica diagram: Journal of Petrology, v. 27, p. 745-750.

Lin, G., Amelung, F., Lavallee, Y., and Okubo, P.G., 2014, Seismic evidence for a crustal magma reservoir beneath the upper east rift zone of Kilauea volcano, Hawaii: Geology, v. 42, p. 187–190.

Lipman, P.W., 1995, Declining growth of Mauna Loa during the last 100,000 years: Rates of lava accumulation vs. gravitational subsidence: Mauna Loa Revealed: Structure, Composition, History, and Hazards Geophysical Monograph Series, p. 45–80.

Lundgren, P., Poland, M., Miklius, A., Orr, T., Yun, S. H., Fielding, E., Liu, Z., Tanaka, A., Szeliga, W., Hensley, S., and Owen, S., 2013, Evolution of dike opening during the March 2011 Kamoamoa fissure eruption, Kīlauea Volcano, Hawai`i: Journal of Geophysical Research, 18 p.

Macdonald, G.A., 1968, Composition and Origin of Hawaiian Lavas: Geological Society of America Memoirs Studies in Volcanology, p. 477–522.

Michael, P. J. & Cornell,W. C., 1998, Influence of spreading rate and magma supply on crystallization and assimilation beneath mid ocean ridges; evidence from chlorine and major element chemistry of mid-ocean ridge basalts: Journal of Geophysical Research, B, Solid Earth and Planets, v. 103, p. 18325-18356.

Montelli, R., Nolet, G., Dahlen, F. A., Masters, G., Engdahl, E. R., & Hung, S. H., 2004, Finite-frequency tomography reveals a variety of plumes in the mantle. Science, v. 303(5656), p. 338-343.

Moore, J.G., and Clague, D.A., 1992, Volcano growth and evolution of the island of Hawaii: Geological Society of America Bulletin, v. 104, p. 1471–1484

Moore, J.G., and Krivoy, H.L., 1964, The 1962 flank eruption of Kilauea volcano and structure of the east rift zone: Journal of Geophysical Research, v. 69, p. 2033–2045.

Moore, J.G., D.A. Clague, and Normark W.R., 1982, Diverse basalt types from Loihi Seamount, Hawaii: Geology, v. 10 (no. 2), p. 88-92.

Murata, K.J., and D.H. Richter., 1966, Chemistry of the lavas of the 1959-60 eruption of Kilauea Volcano, Hawai‘i , U.S. Geological Survey Professional Paper, v. 37-A, p. A1-A26.

Nicholls, J., and Stout, M.Z., 1988, Picritic Melts in Kilauea--Evidence from the 1967-1968 Halemaumau and Hiiaka Eruptions: Journal of Petrology, v. 29, p. 1031–1057.

Nimis, P., 1995, A clinopyroxene geobarometer for basaltic systems based on crystal-structure modeling: Contributions to Mineralogy and Petrology, v. 121, p. 115-125.

Okada, Y., 1985, Surface deformation due to shear and tensile faults in a half-space: International Journal of Rock Mechanics and Mining Sciences & Geomechanics Abstracts, v. 23, p. 128.

Okubo, P.G., Nakata, J.S., and Koyanagi, R.Y., 2014, The Evolution of Seismic Monitoring Systems at the Hawaiian Volcano Observatory, in Poland, M.P., Takahashi, T.J., and Landowski, C.M. eds., Characteristics of Hawaiian volcanoes: Reston, VA, U.S. Department of the Interior, U.S. Geological Survey.

Owen, S., Segall, P., Lisowski, M., Miklius, A., Murray, M., Bevis, M., and Foster, J., 2000, January 30, 1997 eruptive event on Kilauea Volcano, Hawaii, as monitored by continuous GPS: Geophysical Research Letters, v. 27, no. 17, p. 2757–2760.

Peck, D.L., Wright, T.L., and Moore, J.G., 1966, Crystallization of tholeiitic basalt in Alae Lava Lake, Hawaii: Bulletin Volcanologique, v. 29, p. 629–655.

Pietruszka, A.J., and Garcia, M.O., 1999, A rapid fluctuation in the mantle source and melting history of Kilauea Volcano inferred from the geochemistry of its historical summit lavas (1790–1982): Journal of Petrology, v. 40, no. 8, p. 1321–1342.

Pietruszka, A.J., Heaton, D.E., Marske, J.P., and Garcia, M.O., 2015, Two magma bodies beneath the summit of Kīlauea Volcano unveiled by isotopically distinct melt deliveries from the mantle: Earth and Planetary Science Letters, v. 413, p. 90–100.

Poland, M.P., Miklius, A., and Montgomery-Brown, E.K., 2014, Magma supply, storage, and transport at shield-stage Hawaiian volcanoes. In: Poland, M.P., Takahashi, T.J., and Landowski, C.M., 2014, Characteristics of Hawaiian volcanoes: Reston, VA, U.S. Department of the Interior, U.S. Geological Survey, p. 179–234.

Poland, M.P., Miklius, A., Sutton, A.J., and Thornber, C.R., 2012, A mantle-driven surge in magma supply to Kīlauea Volcano during 2003–2007: Nature Geoscience, v. 5, p. 295–300.

Poland, M.P., Sutton, A.J., and Gerlach, T.M., 2009, Magma degassing triggered by static decompression at Kīlauea Volcano, Hawai‘i: Geophysical Research Letters, v. 36, L16306.

Rhodes, J.M., 1995, The 1852 and 1868 Mauna Loa picrite eruptions: Clues to parental magma compositions and the magmatic plumbing system: Mauna Loa Revealed: Structure, Composition, History, and Hazards Geophysical Monograph Series, p. 241–262.

Ryan, M.P., Koyanagi, R.Y., and Fiske, R.S., 1981, Modeling the three-dimensional structure of macroscopic magma transport systems: Application to Kilauea Volcano, Hawaii: Journal of Geophysical Research, v. 86, p. 7111-7129.

Ryan, M.P., 1988, The mechanics and three-dimensional internal structure of active magmatic systems: Kilauea Volcano, Hawaii: Journal of Geophysical Research, v. 93, p. 4213-4248.

Schipper, C.I., White, J.D., Houghton, B.F., Shimizu, N., and Stewart, R.B., 2010, "Poseidic" explosive eruptions at Loihi Seamount, Hawaii: Geology, v. 38, p. 291–294.

Segall, P., Cervelli, P., Owen, S., Lisowski, M., and Miklius, A., 2001, Constraints on dike propagation from continuous GPS measurements: Journal of Geophysical Research, v. 106, no. B9, p. 19301–19317.

Sherrod, D.R., Sinton, J.M., Watkins, S.E., and Brunt, K.M., 2007, Geologic Map of the State of Hawai'i: U.S. Geological Survey Open-File Report 2007-1089, 83 p.

Simkin, T., Tilling, R.I., Vogt, P.R., Kirby, S.H., Kimberly, P. and Stewart, D.B., 2006, This dynamic planet: World map of volcanoes, earthquakes, impact craters, and plate tectonics: US Geological Survey Geologic Investigations Series Map I-2800, 1 two-sided sheet, scale 1: 30,000,000. SIPRE auger. Jon’s Machine Shop (http://jonsmachine. com/), 350, p. 99712-1007.

Stolper, E., Sherman, S., Garcia, M., Baker, M. and Seaman, C., 2004, Glass in the submarine section of the HSDP2 drill core, Hilo, Hawaii: Geochemistry, Geophysics, Geosystems, v. 5(7).

Swanson, D.A., Jackson, D.B., Koyanagi, R.Y., and Wright, T.L., 1976, The February 1969 east rift eruption of Kilauea Volcano, Hawaii: U.S. Geological Survey Professional Paper 891, 33 p.

Thornber, C.R., 2001, Olivine Liquid Relations of Lava Erupted by Kilauea Volcano from 1994 To 1998: Implications for Shallow Magmatic Processes Associated with The Ongoing East-Rift-Zone Eruption: The Canadian Mineralogist, v. 39, p. 239–266.

Tilling, R.I., and Heliker, C.C., 2010, Eruptions of Hawaiian volcanoes: past, present, and future: Reston, VA, U.S. Department of the Interior, U.S. Geological Survey.

Tomiya A., 2000, Depth of magma chamber determined by experimental petrologic methods: World Geothermal Congress, p.1855-1859.

Vinet, N., and Higgins, M.D., 2010, Magma solidification processes beneath Kilauea Volcano, Hawaii; a quantitative textural and geochemical study of the 1969–1974 Mauna Ulu lavas: Journal of Petrology, v. 51, no. 6, p. 1297–1332.

Walker, D., DeLong, S. E. & Shibata, T., 1979, Abyssal tholeiites from the Oceanographer fracture zone; II, Phase equilibria and mixing: Contributions to Mineralogy and Petrology, v. 70, p. 111-125.

Wauthier, C., Roman, D.C., and Poland, M.P., 2016, Joint analysis of geodetic and earthquake fault-plane solution data to constrain magmatic sources: A case study from Kīlauea Volcano: Earth and Planetary Science Letters, v. 455, p. 38–48.

Wolfe, E.W., Garcia, M.O., Jackson, D.B., Koyanagi, R.Y., Neal, C.A., and Okamura, A.T., 1987, The Puu Oo eruption of Kilauea Volcano, episodes 1–20, January 3, 1983, to June 8, 1984, chap. 17 of Decker, R.W., Wright, T.L., and Stauffer, P.H., eds., Volcanism in Hawaii: U.S. Geological Survey Professional Paper 1350, v. 1, p. 471–508.

Wolfe, E.W., Wise, S. W., and Dalrymple, B., 1997, The geology and petrology of Mauna Kea Volcano, Hawaii - A study of postshield volcanism: U.S. Geological Survey Professional Paper 1557, 129 p.

Wright, T. L. & Helz, R. T., 1996, Differentiation and magma mixing on Kilauea's east rift zone: a further look at the eruptions of 1955 and 1960. Part II. The 1960 lavas. Bulletin of Volcanology, v. 57, 602–630.

Wright, T., and Klein, F., 2006, Deep magma transport at Kilauea volcano, Hawaii: Lithos, v. 87, p. 50–79.

Wright, T.L. and Okamura, R.T., 1977. Cooling and crystallization of tholeiitic basalt, 1965 Makaopuhi lava lake, Hawaii: U.S. Geological Survey Professional Paper 1004, 78 p, 1977.

Wright, T.L., and Pierson, T.C., 1992, Living with volcanoes: U. S. Geological Survey Circular 1073, 70 p.

Yang H.J., Frey, F.A., Clague, D.A., and Garcia, M.O., 1994, Submarine lavas from Mauna Kea Volcano, Hawaii: Implications for Hawaiian shield stage processes: Journal of Geophysical Research, v. 99, p. 15,577-15,594.

Yang, H. J., Grove, T. L. & Kinzler, R. J., 1996, Experiments and models of anhydrous, basaltic olivine-plagioclase-augite saturated melts from 0.001 to 10 kbar: Contributions to Mineralogy and Petrology, v.124, p.1-18.

Yang, H.J., Frey, F.A., Clague, D.A., and Garcia, M.O., 1999, Mineral chemistry of submarine lavas from Hilo Ridge, Hawaii: implications for magmatic processes within Hawaiian rift zones: Contrib. Mineral Petrol, v. 135, p. 355-372.

Yoder, H.S. & Tilley, C.E., 1962, Origin of basalt magmas: an experimental study of natural and synthetic rock systems: J. Petrol, v. 3, p. 342–532.

Zerda, C.L., 2016, An Integrated Petrological and Geochemical Approach to Understanding Magmatism Along the East Pacific Rise: Unpublished M.S. thesis, The Ohio State University, Columbus, Ohio.

Zhai, G., and Shirzaei, M., 2016, Spatiotemporal model of Kīlauea's summit magmatic system inferred from InSAR time series and geometry-free time-dependent source inversion: Journal of Geophysical Research: Solid Earth, v. 121, p. 5425–5446.